APPLICATION OF RIGOROUS COUPLED-WAVE THEORY FOR STUDYING RADIATIVE PROPERTIES OF MICRO/NANOSTRUCURES AND SILVER NANORODS ON GRATINGS

A Thesis
Presented to
The Academic Faculty

by

Ahmad M. Haider

In Partial Fulfillment
Of the Requirements for the Degree
Master of Science in the
School of Mechanical Engineering

Georgia Institute of Technology
August 2011

APPLICATION OF RIGOROUS COUPLED-WAVE THEORY FOR STUDYING RADIATIVE PROPERTIES OF MICRO/NANOSTRUCURES AND SILVER NANORODS ON GRATINGS

Approved by:

Dr. Zhuomin Zhang, Advisor
School of Mechanical Engineering
Georgia Institute of Technology

Dr. Yogendra Joshi
School of Mechanical Engineering
Georgia Institute of Technology

Dr. Todd Sulchek
School of Mechanical Engineering
Georgia Institute of Technology

Date Approved: 30th June, 2011

ACKNOWLEDGEMENTS

I wish to thank Dr. Zhuomin Zhang, my advisor for his continuing guidance and encouragement during the entire course of the Master of Science (MS) program. Without his constant help and support, this work would not have been possible on time. I would also like to thank my thesis committee members, Dr. Yogendra Joshi and Dr. Todd Sulchek for their willingness on serving on the committee and taking the time and effort to read the thesis.

I want to thank all the group members for their help and support during various stages of research. I had the opportunity to work with both Mr. Liping Wang and Ms. Xiaojia Wang on separate projects, and both were invaluable experiences. I would also like to take this opportunity to thank them for taking the time to review my thesis manuscript and provide constructive feedbacks. In particular, Mr Liping Wang spent a lot of time with me providing the direction for the first part of the thesis, and I would like to acknowledge his contribution here. Ms. Xiaojia Wang, through her help and discussions on the silver nanorods project, was instrumental in shaping up the second part of the thesis. I would also like to acknowledge the friendship and support of other group members, Mr. Andrew McNamara, Mr. Trevor Bright and Mr. Jesse Watjen. I also appreciate the discussions that I have had with Ms. Nazli Donmezer and Mr. David Lai over one-and-half years of course-work.

Over and above, I am greatly indebted to my family, especially my parents for their love, support, and patience through all these years. Without them, I could not have reached this far. This work is dedicated to them.

TABLE OF CONTENTS

LIST OF TABLES

LIST OF FIGURES

LIST OF SYMBOLS

A	cross-sectional area between parallel plates
a	ridge length in CD gratings
b	Usage 1: separation between two successive plates in parallel plate grating array. Usage 2: groove length in CD gratings
C_{g}	gap capacitance
C_{I}	compensating factor for beamsplitter and different detector responsivities
$\hat{\mathbf{c}}$	unit vector along the optic axis of a silver nanorod
c	speed of light in vacuum
c_1	numerical factor to account for non-uniform charge distribution on capacitor plates
d	Usage 1: total depth of a binary grating structure. Usage 2: diameter of an individual silver nanorod
dL_{r}	reflected radiance
$\mathbf{E}$	electric field vector
f_{r}	bidirectional reflectance distribution function
$\mathbf{H}$	magnetic field vector
h_j	thickness of each rectangular layer in a binary grating
$\mathbf{k}$	wavevector
k_{spp}	x-component of the wavevector for surface plasmon polaritons
L_{i}	incident radiance
L_{k}	Usage 1: kinetic inductance (of drifting electrons). Usage 2: depolarization factor for silver nanorods
L_{m}	magnetic inductance of two parallel plates
l	Usage 1: length of plates in parallel plate grating array. Usage 2: length of an individual silver nanorod.

M	number of rectangular layers in an arbitrary grating profile
m	diffraction order
N	total number of diffraction orders used in RCWA computation
n	refractive index
R_{peak}	peak reflectance of individual diffraction orders computed by RCWA
R_{total}	sum total of all diffraction orders computed by RCWA
R'_{λ}	spectral-directional reflectance
r	*m*th order reflection coefficient for interface between first and second medium
t	Usage 1: *m*th order transmission coefficient for interface between first and second medium (with subscript). Usage 2: plate thickness in parallel plate grating array (without subscript)
V_{A}	signal received by detector A
V_{B}	signal received by detector B
w	plate width in parallel plate grating array
$x_{1,j}$	left abscissa for the *j*th layer in an arbitrary grating profile
$x_{2,j}$	right abscissa for the *j*th layer in an arbitrary grating profile
Z_{tot}	total complex impedance of the LC circuit model

GREEK SYMBOLS

α'_{λ}	spectral-directional absorptance
β	inclination angle of nanorods taken from CD normal
γ	scattering rate of Ag
δ	skin penetration depth
$\delta\Omega_{\text{r}}$	solid angle of receiving area for detector A

ε	electric permittivity
ε_∞	Drude model constant
θ	Usage 1: polar angle (with associated subscript). Usage 2: plate inclinaton of parallel plate grating array (without subscript)
κ	extinction coefficient
Λ	grating period
λ , ω	spectral property in terms of wavelength or angular frequency
μ	magnetic permeability
φ	azimuthal angle
ϕ	Usage 1: generalized volume filling fraction of a material in grating layer. Usage 2: volume filling fraction of silver nanorods on CD
ψ_m	field amplitude for *m*th diffraction order
$d\omega$	elemental solid angle
ω_p	Usage 1: plasma frequency of Al. Usage 2: plasma frequency of Ag

SUBSCRIPTS

0	free space
CD	compact disc
E	extraordinary
eff	effective
i, inc	incidence
m	*m*th diffraction order
O	ordinary
proj	projected

R, 1	fundamental MP resonance
r	reflection
x	x-component
x,m	x-component for *m*th order
z	z-component
z,m	z-component for *m*th order

LIST OF ABBREVIATIONS

f	non-dimensionalized volume filling fraction
AgNR	silver nanorod
BG	Bruggeman (Effective medium theory)
BRDF	bidirectional reflectance distribution function
CD	compact disc
DHR	directional-hemispherical reflectance
EMT	effective medium theory
FWHM	full width at half maximum
IS	integrating sphere
LP	long plates
MG	Maxwell-Garnett (Effective medium theory)
MMM	multilayer modal method
MP	magnetic polariton
PTFE	polytetrafluoroethylene
RCWA	rigorous coupled-wave analysis
SERS	surface enhanced raman scattering

SP	short plates
SPP	surface plasmon polariton
TAAS	three-axis automated scatterometer
TE	transverse electric
TM	transverse magnetic
W.A	Wood’s anomaly

SUMMARY

Tailoring the radiative properties of periodic micro/nanostructures can be used as an efficient way to create devices which have applications in energy harvesting, bioengineering and optical sensing. Analysis of these structures is typically performed by either an approximation or a rigorous solution of the electromagnetic wave phenomena at the interfaces. The thesis explores the application of rigorous coupled-wave analysis (RCWA) method to study the optical responses of microstructure arrays.

The first part of the thesis elucidates the various mechanisms responsible for causing enhanced light absorption in inclined parallel plate grating arrays which cause them to act as resonators. Parallel plate resonators have been widely used for surface impedance measurements of high-temperature superconductor films. Wood's anomaly (W.A), surface plasmon polariton (SPP) resonance and magnetic polariton (MP) resonance phenomena are discussed with regard to both long and short plate lengths. Illustrative evidences of SPP and MP resonances are provided through electromagnetic field distributions, spectral-directional contour plots and polar plots computed by RCWA method. Analytical agreement with visual data is obtained through use of a LC circuit model. The effects of different geometric parameters on the magnetic resonance conditions are investigated through the use of both RCWA and LC circuit model.

The second part of the thesis deals with application of RCWA to study the effect of light scattering on inclined silver nanorod (AgNR) arrays grown on compact disc (CD) substrates. AgNR arrays have been previously studied by other researchers for their optical responses such as Surface Enhanced Raman Scattering (SERS) effect for

biological applications. In the present study, AgNRs exhibit diffraction characteristics due to the gratings present in the underlying CD layer. Depending on the manner in which AgNRs are oriented with respect to CD gratings, they exhibit different optical behavior to incoming light. Effects of both incident light polarization and AgNR orientation with respect to the substrate are studied. Effective medium theory is used to calculate the effective properties of AgNR-air layer. Calculated results are compared with experimental values and good agreements are observed for total reflection as well as trends of individual diffraction orders.

CHAPTER 1

INTRODUCTION

Tailoring the radiative properties of micro/nanostructured surfaces through structural and/or optical modification has been an active area of interest in recent years. They have tremendous uses in energy conversion applications, photonics, diffraction gratings, thermophotovoltaic devices, solar cells, drug delivery systems and many others [1-3]. They are also extensively used in biological sensing applications and can enhance the sensitivity for some chemical and biological binding events by up to a factor of 10^9 [4]. A nanorod-mediated surface plasmon resonance sensor for sensitivity enhancement is an example of an application in this direction [5]. Characterizing the radiative properties of these surfaces becomes very important as they control much of the morphological dependent phenomena such as wettability, SERS and photonic bandgap [6].

Micro/nanostructures, including diffraction gratings and its various modifications, have been the source of numerous applications in the fields of integrated optics, holography, spectral analysis and optical data processing among others [7]. Diffraction gratings are periodic media known to behave differently from other rough surfaces in that they diffract incident light in certain directions, instead of scattering it over the entire space. This property, which is a direct function of periodicity and wavelength, has made them famous in spectroscopic applications [8]. Gratings are also modified for many other applications such as arrayed waveguides which are used in input-output coupling thereby increasing transmission capacity of optical fibers [9, 10]. They can be combined with stacks of dielectric layers for hostile-environment protection

or to reduce absorption losses, as done in high-power laser pulse compression methods [11, 12]. Gratings made of modulated metallic and dielectric layers are used in X-ray domain for focusing and beam shaping. One can introduce anisotropy, chirality or nonlinearity into the gratings to excite guided or surface waves in order to enhance various nonlinear effects [13, 14]. They are also used for precise control of light propagation and emission in photonic devices, in which photonic bandgaps are created by arranging metallic or dielectric particles in a periodic lattice [15]. Another kind of diffraction gratings, known as crossed gratings, have modulations of refractive indices in two or three directions [16].

Micro/nanostructures have been studied by many groups for their reflection and transmission behavior. In 1971, Neviere was one of the first authors who were able to map the grating surface to a plane and, later on, were able to predict diffraction efficiencies or DEs (implying energy distribution via reflectance or transmittance) for each order [17-19]. Soon after, Maystre et al. performed an analysis of reflection diffraction efficiencies of blazed and holographic gratings for different blazing angles [20]. Following these preliminary works, many authors started working on both design as well as fabrication methods of gratings with the objective of achieving high diffraction efficiencies [21-23]. By 1989, high efficiency, high dispersion diffraction gratings were being designed based on total internal reflection principles, which were independent of both grating shape and material [24]. In 1995, through computational and experimental measurements, Li demonstrated the use of compressor diffraction gratings, which exhibit very high first order reflection efficiency, for use in high-power laser applications [12].

In 1997, Ebbesen et al. demonstrated that sub-wavelength hole arrays can exhibit unusually high transmission efficiencies which fall well outside the predictions [25]. Soon after, Pendry et al. [26], through a theoretical analysis of the transmission response of deep and narrow slits on metallic gratings, showed that near perfect transmittances can be obtained at certain incident wavelengths. He attributed this due to either resonance caused by surface plasmons or coupling of incident waves with waveguide resonances of the slit. At this time, two-dimensional evanescent waveguide arrays were also fabricated and studied by Pertsch who was able to demonstrate ideal discrete diffraction [27]. Labeke and Baida [28], in their study of spectral response of metallic films with engraved 2D periodic structure of annular aperture arrays, achieved enhanced transmission of up to 90% which they attributed to guided modes inside the subwavelength coaxial structure. From the study of optical transmission behavior of hole arrays perforated in trilayer structures, Li et al. proposed the concept of magnetic polaritons indicating coupling between incident light and magnetic resonance inside subwavelength periodic structures [29, 30]. Wang and Zhang elucidated the effect of magnetic polaritons on the radiative properties of double layer nanoslit arrays, and used a LC circuit model to prove their existence [31]. Lee and Zhang [32] studied the confinement of infrared radiation to nanometer scales through metallic slit arrays. They also analyzed the transmission enhancement through nanoscale metallic slit arrays from visible to infrared spectrum. Depending on the spectral region analyzed, they attributed the enhancement to Wood's anomaly, cavity resonance and the effective-medium behavior [33].

At the same time, several groups focused their efforts on efficient fabrication techniques for the synthesis of microstructures. Novel techniques such as glancing angle

deposition [34], nanolithography [35], X-ray lithography, soft lithography [36] and monolayer colloidal crystal (MCC) template approaches [37] were invented. These techniques have the advantages of high resolution, high repeatability, flexibility and ability to fabricate ordered microstructured arrays with controllable morphologies. These improved methods have enabled researchers to work on nanostructure applications which can now be easily fabricated and mass replicated.

The thesis is primarily focused on numerical studies on the radiative properties of different types of micro/nanostructured arrays. The work focuses on two types of nanostructures: inclined parallel plate aluminum gratings on an aluminum substrate and inclined silver nanorods grown on planar gratings formed by compact discs.

Diffraction of a plane electromagnetic wave by inclined parallel plate sub-micron gratings is numerically treated by the use of RCWA technique. The effects of various resonance mechanisms responsible for enhancing the absorption behavior of these structures are considered. Two-dimensional electromagnetic field plots and spectral-directional contour plots help to visualize the light entrapment phenomenon achieved through the different resonance mechanisms. LC circuit model is described and used to analytically predict the magnetic resonance frequencies. The effects of plate length, plate thickness, inclination angles and grating period on the magnetic resonance frequency are investigated, through both RCWA and LC circuit models.

The other types of nanostructures are silver nanorod arrays which are anisotropic in nature due to their high-aspect ratios. However, with a few reasonable assumptions, they can be assumed to be behaving isotropically. Firstly, the nanorods-on-CD structures are subjected to diffraction measurements to measure their radiative properties. Then

quantitative methods such as RCWA and effective medium theory are used to calculate their radiative properties, in order to obtain a qualitative agreement with the measured values.

These studies help us gain a fundamental understanding of the radiative properties of engineered micro/nanostructures from their scattering, absorption and resonance behavior and will facilitate the design and applications of similar structures.

CHAPTER 2

THEORETICAL BACKGROUND AND NUMERICAL METHOD

2.1 Review

Since 1930, many physicists, starting with Rowland, have attempted to solve the problem of finding the light distribution within a given diffraction order with various approximation techniques. Exact solutions of Maxwell's electromagnetic equations were not possible before the advent of high-speed computers, and hence earlier work focused mainly on scalar approximations (wavelength greater than grating period). It was only in 1956 when Meecham [38] followed by Stroke (1960) [39] was able to formulate a rigorous solution for an infinitely conducting surface. Their solution, based on an integral formalism, focused mainly on TE wave polarization and was applicable only for shallow grooves with sharp discontinuities, as was later shown by Petit and Cadilhac [18]. Here TE waves are defined as the case when electric field vector is perpendicular to the plane of incidence which is defined by the surface/interface normal and incident light's wavevector. For TM waves the same condition holds for magnetic field vector instead of electric field vector. The next major development was proposed in 1972 by Maystre when he expanded the solution's usefulness to include materials with finite conductivities [20]. He came up with single integral equation formalism that could handle real metals with no geometric restrictions. He compared these results to those with infinite conductivity and found significant differences in reflectivity for TE waves.

On the other hand, Neviere et al. [18, 19] discovered a differential formalism for the solution of Maxwell's equations that would not only lead to same results as above, but also apply to dielectric coatings. It could also handle other concave shaped periodic

diffracting structures such as cylinders and grating couplers. This was called the classical differential method, which was much simpler and worked fine for both TE and TM polarizations in the case of dielectric gratings. However accurate results were only obtainable for TE polarization in case of highly reflective metallic gratings with deep grooves. For TM polarization, the solution suffered from poor convergences with respect to number of spectral orders as well as numerical instability for some groove depths and metal conductivity, thus violating energy balance. The instability was claimed to be due to numerical integration process that was used in differential formalism. To counter the instability due to integration process, a special technique for rectangular profiles was developed in 1981 called the rigorous coupled-wave analysis or RCWA [40-43]. This technique, popularized by Moharam and Gaylord, bypassed the integration process altogether with an eigenvalue technique. It was later extended to arbitrary profiles through staircase approximation. However, this method also suffered from lack of convergence for TM polarization and was limited to special profiles.

The first breakthrough in solving the stability issue came in 1990 when Tayeb [44] was able to use an orthonormalization procedure to avoid shrinking of Fourier space dimensions during integration process. This work spurred several other approaches which worked to ensure the solution's stability, notable among them being the 'S-matrix propagation algorithm' [45]. These approaches when combined with RCWA method completely eliminated the stability issue. The second breakthrough came when Lalanne and Morris [46] were able to improve the convergence issue by reformulating the wave propagation equations . Surprisingly, the method worked well on lamellar gratings but did not for sinusoidal profiles. The explanation was provided by Li [47, 48] who studied

the convergence behavior of truncated Fourier series of two continuous or discontinuous functions, and found that the propagation equations became ill-suited when truncated in the Fourier space. He was able to propose appropriate factorization rules which were used to improve the propagation equations when being truncated. After including all these improvements, rigorous coupled-wave analysis is currently able to solve for energy distribution in any diffraction order for both TE and TM polarizations and is applicable for both metallic and dielectric gratings with arbitrary profiles and depths.

2.2 Theory of Rigorous Coupled-wave Analysis

The rigorous coupled-wave theory is widely used for diffraction analysis of micro/nanostructured surfaces of arbitrary shapes and dimensions. It is an exact solution of Maxwell's electromagnetic equations and the accuracy of the solution depends solely on the number of retained terms in the space-harmonic expansion of the fields in the diffracting structures. It also satisfies the principle of conservation of energy [49, 50]. The following paragraphs outline the principle of rigorous coupled-wave theory for both TE and TM polarizations when applied to diffraction gratings.

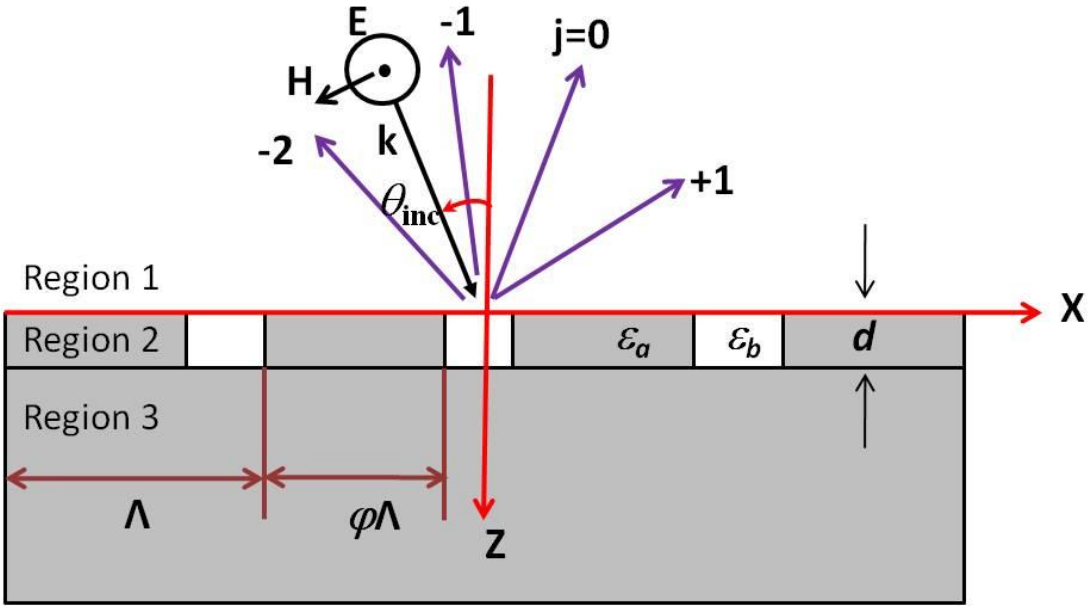

Figure 2.1 Schematic of diffraction of electromagnetic radiation by a grating (for TE wave)

Figure 2.1 shows a plane electromagnetic wave of wavelength λ is incident at an angle θ_{inc} on the grating structure, with the plane of incidence being perpendicular to the grooves. According to Huygens principle, this incident wave results in many reflected waves at the point of incidence. Region 1 is free space with an electric permittivity of ε_1 =1 where $\varepsilon = (n + i\kappa)^2$, n being the refractive index and κ being the extinction coefficient. Region 3 is also a homogenous medium with electric permittivity ε_3. Region 2 is the grating layer and is a heterogeneous medium, whose permittivity is a periodic function of x, i.e. $\varepsilon(x + \Lambda) = \varepsilon$. The dielectric function in the ridges is ε_a where as dielectric function in the grooves is ε_b, as shown in the figure above.

Let k_{1x} be the x component of the incident wavevector $\mathbf{k_1}$ and k_{1z} be its z component. The magnitude of the wave vector is given by

$$k_1 = \frac{2\pi n_1}{\lambda} = \frac{2\pi}{\lambda} = k \tag{2.1}$$

Similarly for region 3,

$$k_3 = \frac{2\pi n_3}{\lambda} = n_3 k \tag{2.2}$$

For a TE wave, the normalized incident electric field is given by

$$\mathbf{E} = \exp\left(ik_{1x}\, x + ik_{1z}\, z\right)\hat{\mathbf{y}}\ , \tag{2.3}$$

where $\exp(-i\omega t)$ term has been dropped for this and all subsequent instances. For each of the diffracted waves, the *x* component of their wave vectors is given by the Bloch-Floquet condition which is applicable inside a periodic structure,

$$k_{x,m} = \frac{2\pi \sin\theta}{\lambda} + \frac{2\pi}{\Lambda} m, \tag{2.4}$$

where m is order of the diffracted wave. Phase matching conditions specify that tangential components of electric and magnetic fields should be continuous across an interface. Because of the phase matching condition, k_x must be same in all the media. We can calculate $k_{z,m}$ for the first medium by using the relation

$$k^2 = k_{x,m}^2 + k_{z,m}^2 \tag{2.5}$$

Similarly, $k_{z,m}$ for second and third media is calculated by using eq. (2.5) with the corresponding wavevectors. Clearly if $k_{x,m} > k_1$, $k_{z,m}$ will be purely imaginary and the *m*th order diffracted wave will decay exponentially towards *z*-direction and become an evanescent wave.

Total magnitude of electric field in region 1 is given by superimposition of incident and reflected waves as,

$$E_1(x,z) = \exp\left(ik_x x + ik_{1z} x\right) + \sum_m r_m \exp\left(ik_{x,m} x - ik_{1z,m} z\right), \tag{2.6}$$

where r_m is the reflection coefficient for the interface between first and second medium. Similarly, total electric field in region 3 is given by superimposition of all transmitted waves as

$$E_3(x,z) = \sum_m t_m \exp\left(ik_{x,m} x + ik_{3z,m}\left(z - d\right)\right), \tag{2.7}$$

where t_m is transmission coefficient for *m*th order transmitted wave.

The electric field in grating layer $\mathbf{E_2}$ can be expanded in terms of its space harmonic components due to the periodicity. These components are phase matched with the diffraction orders in the first and third regions. Normalized form of $\mathbf{E_2}$ is

$$E_2(x,z) = \sum_m \psi_m(z) \exp\left(ik_{x,m} x\right), \tag{2.8}$$

where ψ_m is the field amplitude for the *m*th diffraction order. Also, because relative permittivity in the grating layer is a periodic function with the period Λ, it can be expanded in terms of a Fourier series as

$$\varepsilon(x) = \sum_u \varepsilon_u \exp\left(\frac{i2u\pi}{\Lambda} x\right), \tag{2.9}$$

where ε_u is the *u*th Fourier coefficient given by

$$\varepsilon_0 = \phi\varepsilon_a + (1-\phi)\varepsilon_b \quad \text{and} \quad \varepsilon_u = \frac{(\varepsilon_a - \varepsilon_b)\sin(u\phi\pi)}{u\pi} \tag{2.10}$$

Here ϕ is the filling fraction of material A in the grating layer.

To obtain the wave equation for the electric field in the grating layer, one needs to solve the Maxwell's equations. However, since the layer is non-homogeneous, the wave equation becomes

$$\nabla^2\mathbf{E}_2 + \nabla\left(\mathbf{E}_2 \bullet \nabla \ln\varepsilon\right) + \nabla \ln\mu \times \left(\nabla \times \mathbf{E}_2\right) + k^2\mu\varepsilon\mathbf{E}_2 = 0 \tag{2.11}$$

Since $\mathbf{E}_2$ is along *y*-direction and $\nabla \ln\varepsilon$ is non-zero only along *z*-direction, their dot product results in 0. Also μ=1 as the medium is nonmagnetic. Hence the wave equation becomes

$$\nabla^2 E_2(x,z) + k^2\varepsilon(x)E_2(x,z) = 0 \tag{2.12}$$

Equations (2.7) and (2.8) are substituted into (2.12) to yield the final coupled wave formulation

$$\sum_m \left(\frac{d^2\psi_m}{dz^2} - k_{x,m}^2\psi_m + k^2\sum_p \varepsilon_{m-p}\psi_p \right) \exp(ik_{x,m}x) = 0 \tag{2.13}$$

This equation has to be satisfied for every *m*th term and hence the coefficients of $\exp(ik_{x,m}x)$ must be identically zero for each term. Equation (2.13) is a set of second order coupled difference-differential equations where each space harmonic term is coupled to other terms through the harmonics of the grating. The numerical solution is obtained with sufficiently large number of diffraction orders.

The magnetic field in region 2 is obtained from Maxwell's equations:

$$\nabla \times \mathbf{E} + \frac{\partial(\mu\mathbf{H})}{\partial t} = 0 \tag{2.14}$$

where μ = 1 is the magnetic permeability of region 2. Based on the form of electric field given in equation (2.8), magnetic field in region 2 is expressed as

$$H_{2,x} = \frac{i}{\omega\mu}\sum_m k\gamma_m(z)\exp(ik_{x,m}x) \tag{2.15}$$

$$H_{2,z} = \frac{1}{\omega\mu}\sum_m k_{x,m}\psi_m(z)\exp(ik_{x,m}x) \tag{2.16}$$

where γ_m and ψ_m are related by

$$\frac{d\psi_m(z)}{dz} = k\gamma_m(z) \tag{2.17}$$

To solve the above equation, we need another relation between γ_m and ψ_m. It can be obtained by substituting eq. (2.15), eq. (2.16) and eq. (2.8) into the following equation

$$\nabla \times H - \frac{\partial(\varepsilon E)}{\partial t} = 0 \tag{2.18}$$

From eq. (2.18), we obtain another set of relationships between γ_m and ψ_m, which upon expansion yields,

$$\frac{\partial \gamma_m(z)}{\partial z} = \left(\frac{k_{x,m}^2}{k} \psi_m(z) - k \sum_n \varepsilon_{(m-n)} \psi_m(z) \right) \tag{2.19}$$

Solution of (2.17) and (2.19) is expressed in matrix form as

$$\left[\frac{\partial^2 \Psi}{\partial (kz)^2} \right] = [\mathbf{A}][\Psi] \tag{2.20}$$

Here Ψ is the matrix of $\psi_m(z)$. If the diffraction orders are given as $m = 0, \pm 1, \pm 2, ..., \pm q$, then $N = 2q+1$ is the total number of diffraction orders and the size of matrices Ψ and $\mathbf{A}$ are $N \times N$. Also, $\mathbf{A}$ is defined as

$$\mathbf{A} = \mathbf{K}_x^2 - \mathbf{E}' \tag{2.21}$$

$\mathbf{K}_x$ is a diagonal matrix whose elements are given by $\mathbf{K}_x(a,a) = \frac{k_{x,(a-q-1)}}{k}$ and $\mathbf{E}'$ is a $N \times N$ matrix formed by the Fourier coefficients of the dielectric function. Eq. (2.20) is solved by eigenvalue analysis and application of relevant boundary conditions. This work is focused primarily on the application of RCWA code to arbitrary grating profiles.

2.3 RCWA Implementation for an Arbitrary Grating Profile

In the present thesis, RCWA has been used to calculate the directional-hemispherical reflectance of binary diffraction gratings.

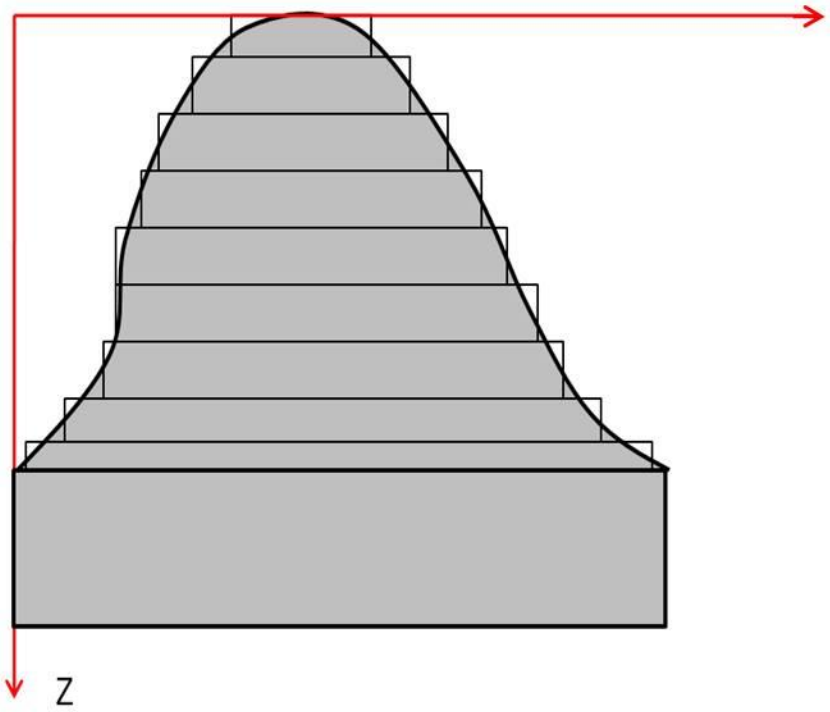

Figure 2.2 Arbitrary binary grating profile which has been approximated by multiple rectangular binary gratings

Figure 2.2 shows an arbitrary profile grating which is broken into multiple rectangular slices such that each slice is parallel to the substrate and can be treated as a binary diffraction grating by itself. As the number of slices increase, these slices closely approximate the actual profile. Each layer is numbered from top to bottom, the 1st layer being topmost layer and z_j is the z coordinate for the center of *j*th layer. Given that total

grating depth is d and assuming each layer to be equally thick, then thickness of each layer can be computed by

$$h_j = z_j - z_{j-1} = \frac{d}{M} \tag{2.22}$$

for the jth layer where M is the total number of rectangular slices. Based on this definition

$$z_j = (j-1)h_j + \frac{h_j}{2},\ j = 0,1,...M \tag{2.23}$$

The width of each layer is so chosen such that the actual grating profile bisects the vertical edges of the rectangular slices [48]. The left and the right x coordinates, or abscissas for jth layer, are defined as $x_{1,j}$ and $x_{2,j}$, respectively. Depending on the actual grating profile, the values of abscissas may change significantly. The electric permittivities may also depend on j, but within each layer they are piecewise constant:

$$\varepsilon_j(x) = \begin{cases} \varepsilon_{2.j},\ x_{1,j} \le x \le x_{2,j} \\ \varepsilon_{1,j},\ otherwise \end{cases} \tag{2.24}$$

In the analysis considered in this thesis, the magnetic permeability of each layer μ_j is assumed to be unity. Along with the above parameters, the dielectric constants of the grating structure and the surrounding media are required as inputs to the RCWA program. The RCWA utility is coded in MATLAB and can calculate the total directional-hemispherical reflectance and transmittance, spectral-directional reflectance and transmittance for each diffraction order, as well as plot both the actual profile and the approximated profile of the given microstructure for profile verification. The code has been validated by comparison with several publications. Two specific validation cases are included below: dielectric rectangular gratings and triangular metallic gratings.

2.4 Code Validation

2.4.1 Validation for rectangular profile dielectric gratings

The RCWA program is validated against the results published by Moharam and Gaylord [49] who performed the diffraction analysis of one-dimensional binary gratings with rectangular profiles as illustrated in fig. 2.3. The grating period is equal to wavelength and the refractive index of the grating layer as well as the substrate is 2.04. The incident medium is air (refractive index =1).

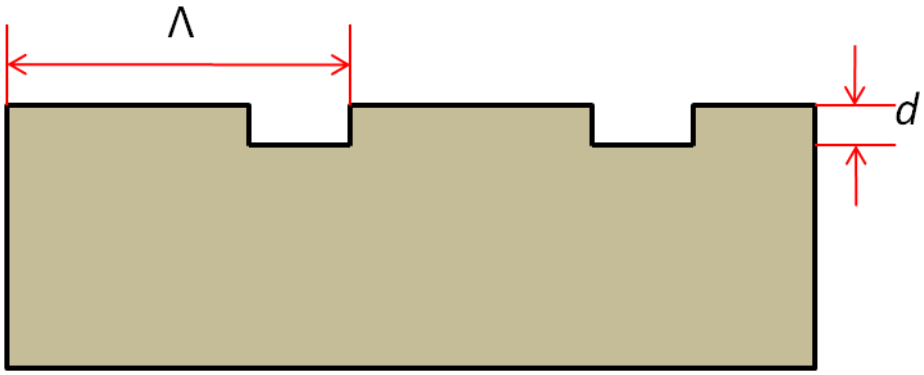

Figure 2.3 One-dimensional rectangular binary grating made of a dielectric material, having a depth *d* and period Λ. These are deep gratings with depth as much as 5 Λ

The first order diffraction efficiencies are validated against the RCWA program for planar polarization cases (TE and TM waves) only in fig 2.4. It can be seen that the agreement is very good even for gratings which are 5 Λ deep. For this calculation, 101 Fourier diffraction orders are used. The relative difference between using 151 and 101 orders is less than 2% and hence 101 orders are deemed to be sufficient.

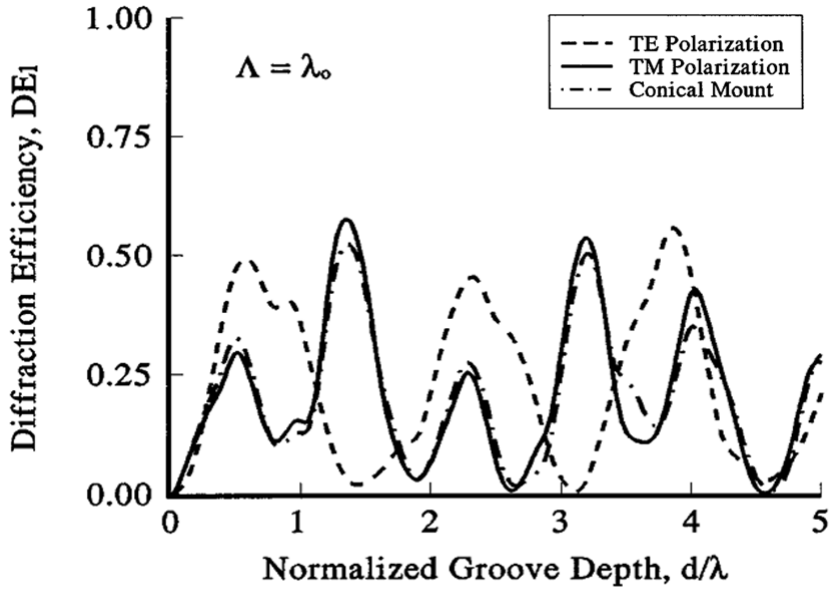

(a)

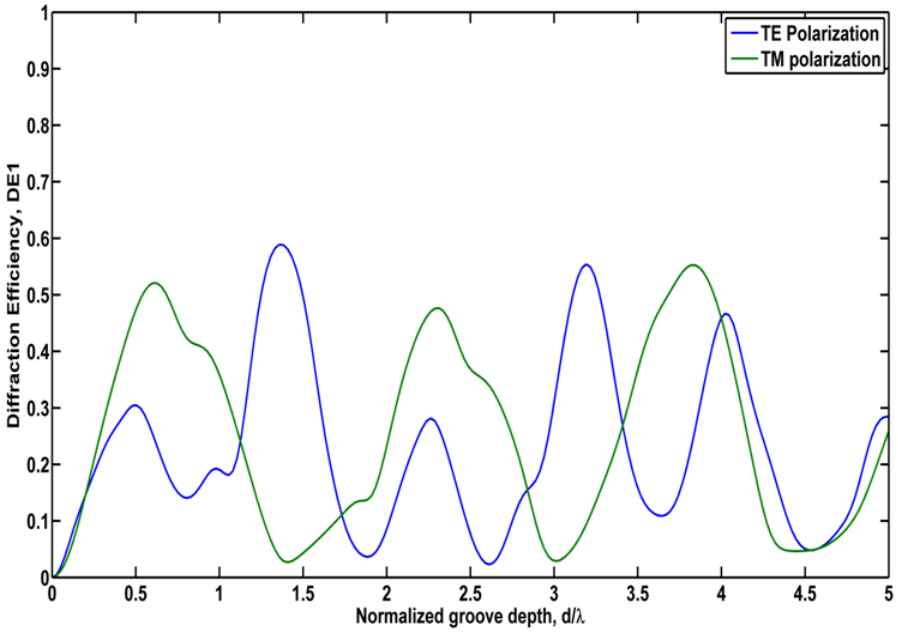

(b)

Figure 2.4 Validation of first order diffraction efficiencies of deep dielectric gratings in (a) published results against (b) RCWA program for TE and TM polarizations.

2.4.2 Validation for arbitrary profile metallic gratings

The RCWA program is validated against results obtained by R-matrix multilayer modal method (R-matrix MMM) followed by Li [48]. The grating approximates a right angled triangle whose period is 0.8233 um and depth is 0.341 um. Refractive index of silver is $(0.1+5.58i)^2$ while the refractive index of medium is 1.96. Wavelength and number of diffraction orders used are 0.85 um and 51, respectively. The grating profile and sample results are shown below. To simulate the exact conditions in [48], only 4 layers are used to model the profile. However, the diffraction efficiency does not change appreciably on using more layers (=20) or higher number of diffraction orders (=101).

Figures 2.5 (a) and (b) below depict the actual geometrical profile of the triangular grating and a MATLAB plot of the grating itself for plot verification. Figures 2.6 (a) through (d) show the comparison of DE's calculated from RCWA with results achieved through R-matrix MMM method. RCWA is able to simulate the same trends and values for individual diffraction orders as well as the sum of all diffraction orders. Hence one can reasonably assume that the RCWA code can be used to predict the refletances/transmittances of diffraction microstructures of arbitrary shapes and materials.

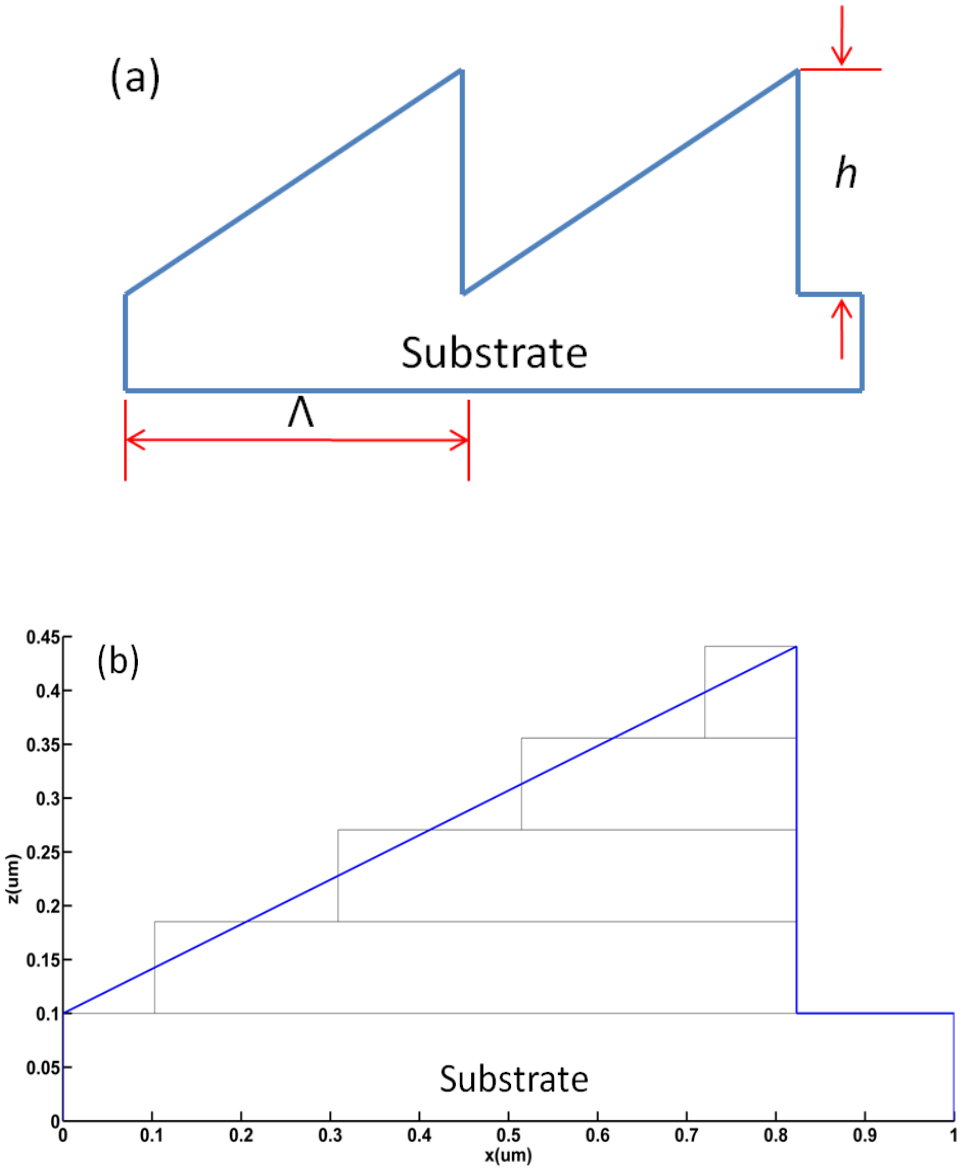

Figure 2.5 (a) A metallic binary grating with triangular profile used for validating RCWA program against published results (b) MATLAB plot of the grating showing the decomposition of triangle (shown in blue) into 4 rectangular layers (shown in black). The MATLAB profile plots are part of RCWA program

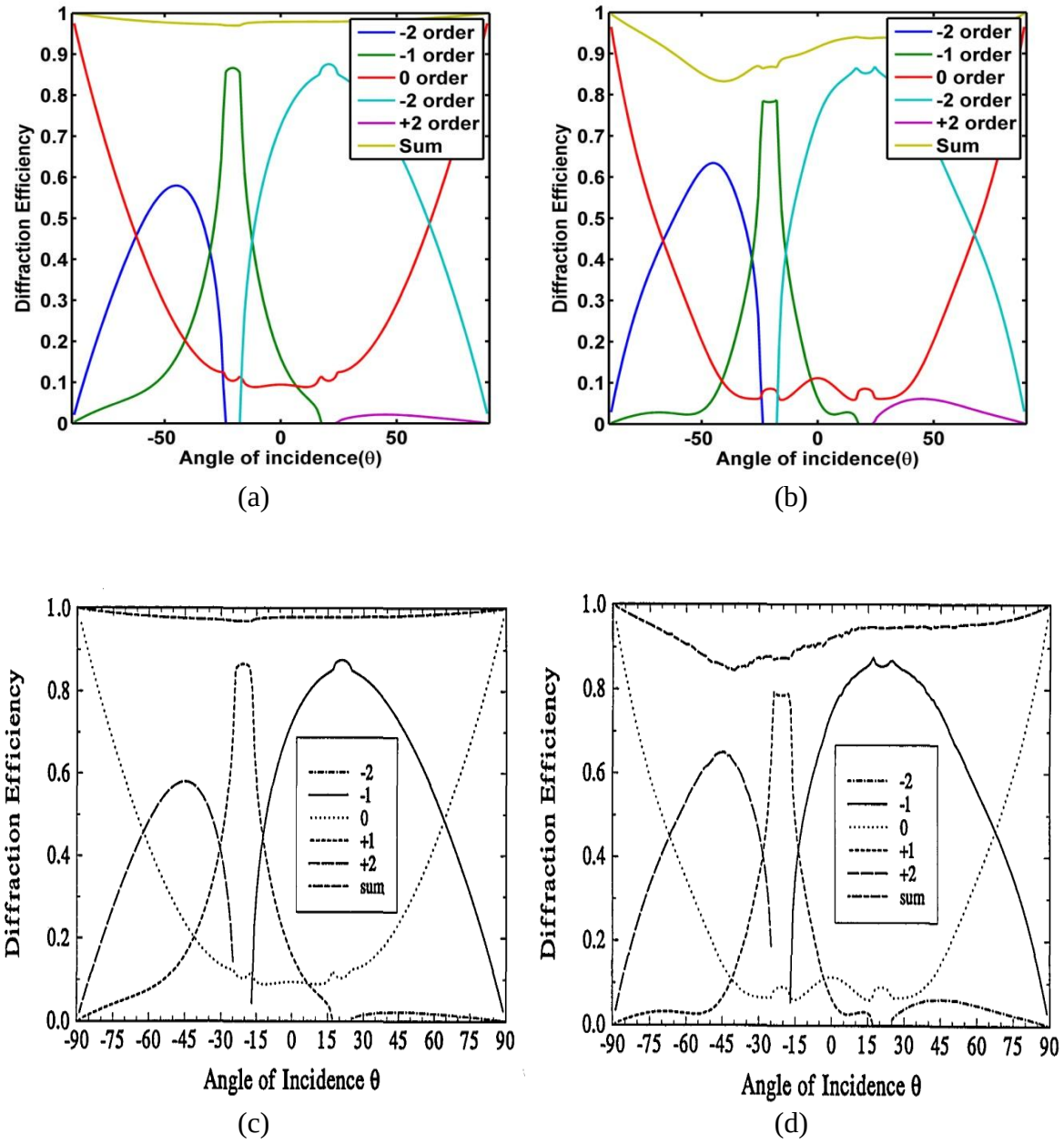

Figure 2.6 Diffraction Efficiencies of different orders for a silver four-level binary grating in TE (left) and TM polarizations (right). Figures (a) and (b) are obtained from RCWA calculations while (c) and (d) are obtained by R-matrix MMM

CHAPTER 3

RADIATIVE PROPERTIES OF MICRO/NANOSTRUCTURES

3.1 Introduction

Spectral control of thermal radiation by micro/nanostructures has been the focus of research in radiative heat transfer since the last decade. It becomes an important issue while designing energy-efficient devices or minimizing energy consumption in heating and lighting systems. Generally spectral control can be achieved by multilayer coatings [51]. However devices utilizing spectrally controlled optical properties, such as thermophotovoltaic (TPV) devices and solar absorbers, are often operated in high-temperature environments, where these coatings are quickly degraded [52, 53]. In such cases, periodic surface microstructures with tailored spectral radiative properties can be considered as an attractive option to multilayer coatings. Periodic microstructures also have many advantages such as adjustable structural shape and period as well as freedom of choice of material [54].

Recent developments in the fields of microfabrication, such as nanolithography [35] and monolayer colloidal crystal methods [37], have made it possible to design structures with sub-wavelength dimensions. Resonance effects between incident light and periodic micro/nanostructures have been utilized to achieve spectral control of the radiative properties of these structures. Hesketh and Zemel [55, 56] and Wang and Zemel [57, 58] have reported on polarized spectral emittance from one-dimensional silicon lamellar gratings. Buckius [59] has published a detailed paper on reflectance from two-dimensional metallic gratings. Heinzel et al. [60] have utilized thermal radiation from microstructured W surfaces to fabricate TPV selective emitters.

3.2 Mechanisms Responsible for Extraordinary Optical Behavior

The effect of resonance on the optical behavior of microstructures has been studied by many research groups. Petit and Maystre [20] were one of the earlier authors who performed theoretical and numerical studies to understand grating anomalies linked to energy absorption. They discussed absorption due to excitation of surface plasmon polaritons [61], which occur at interfaces between dielectric and metals and are responsible for enhanced transmission/emission. Sensors based on SPPs have been fabricated and studied by many groups such as Kim et al. [62] who used periodic metallic nanowires, and Quinn et al. [63] who developed SPP resonance-based biosensors for detection of cell-ligand interactions. Other forms of resonance such as Wood's anomaly and cavity resonance are also responsible for enhanced transmission and absorption in some cases. Wood's anomaly [64], named after R.W. Wood, was discovered when he observed narrow spectral regions on many diffraction gratings which showed a sharp change of diffracted energy. The anomaly occurs when a diffraction order shows up at the grazing angle. The power which would have otherwise been sent into the forbidden region was redistributed among the propagating orders, resulting in genuine enhancement of reflection efficiency. There have been multiple studies on the effects of Wood's anomaly on both reflectance and transmittance spectra of gratings [33]. On the other hand, cavity resonance occurs when standing waves exist in cavities formed by the gratings. At resonance conditions, strong electromagnetic fields exist inside the grating which subsequently enhances the structure's reflection/transmission efficiency, as observed in subwavelength nanoslit arrays [33]. Another concept which can enhance light absorption are magnetic polaritons, proposed by Li [29, 30] which represent coupling

between incident light and magnetic resonances inside subwavelength periodic structures. MPs are used to realize optical negative-index metamaterials, with applications such as superlens [31]. It should be noted that while SPP's and MP's are valid only for TM waves, cavity resonance and Wood's anomalies can occur for both TE and TM waves.

3.3 Inclined Parallel Plate Grating Array

Inclined parallel plate grating arrays have been previously used to demonstrate the spectral control of radiative properties of micro/nanostructures through their filter and resonator characteristics [65]. However, most of the previous studies introduced some form of approximation while obtaining the radiative properties. Kobayashi et al. performed theoretical studies on the diffraction behavior of inclined parallel plate grating by Weiner-Hopf technique, and were able to derive asymptotic solutions [66]. They also studied plane wave diffraction by open-ended parallel plate waveguide cavity [67] via the same technique to obtain approximate solutions. Cornet et al. investigated the conical diffraction behavior of inclined grating by rigorous differential methods, but he assumed the walls to be perfectly conducting [65].

This study focuses on a rigorous numerical investigation of the thermal radiative properties of inclined parallel plate grating array using RCWA in a broad spectrum range from 0.1 μm (ultraviolet) to 8.0 μm (infrared). Two types of plates: short plates (plate length < grating period) and long plates (plate length > grating period) are considered. Effect of SPP resonance and MP resonance to achieve high absorptance is demonstrated with one-dimensional spectral plots and two-dimensional spectral-directional contour plots of wavelengths and incidence angles. Kirchoff's law can be used to link the

absorptance to emittance [68] and hence these structures can also be good emitters. Electromagnetic field plots are used to show confinement of magnetic field, and hence light entrapment, caused by the resonance in these structures. Also, validity of MP resonance is further confirmed by quantitative evidence provided by an approximate LC circuit model of the structure. Finally, a parametric study is conducted which illustrates the effect of geometric parameters, such as plate length, plate thickness, inclination angle and grating period on the radiative properties of these micro/nanostructures.

3.4 Numerical Study

3.4.1 Geometry

In the present work, the plane of the paper is assumed to be the *X*-*Z* plane, and *Y*-direction is into the plane of the paper. The cross section of the inclined parallel plate grating array is in *X*-*Z* plane and is assumed to be infinitely extended into the *Y*-direction. Aluminum (Al) is selected as the grating material as well as the material for the semi-infinite substrate. The parallel plates are separated by air. Λ is the grating period; l is the plate length; t is the plate thickness and θ is the inclination angle of the plates. A schematic of the plate array is shown in fig. 3.1 below for reference.

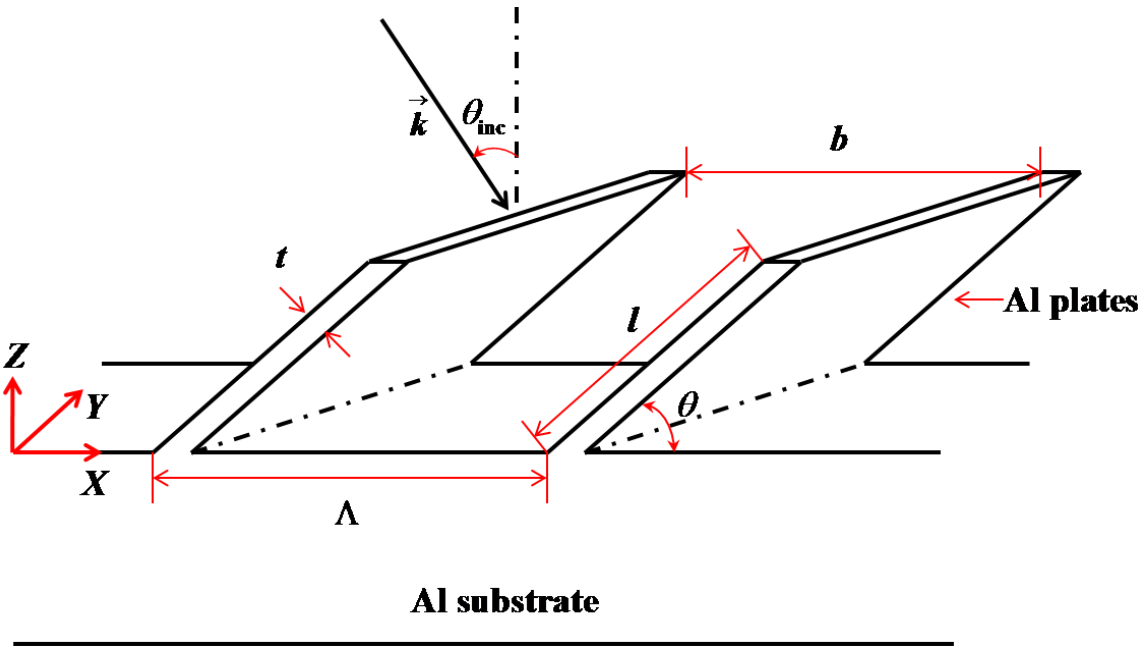

Figure 3.1 Schematic of an inclined parallel plate grating array made of aluminum (Al) placed in air

3.4.2 Radiative properties at normal incidence

The grating period is taken to be Λ=555 nm and the inclination angle is set to θ = 26.75º. The lengths of the plates are $l_1 = 1.5\Lambda = 832.5$ nm, $l_2 = 0.5\Lambda = 277.5$ nm, for the long plates (LP) and the short plates (SP) respectively. Plate thickness t = 100 nm is the same for both structures. Based on the above defined geometry, successive plates are separated by a distance $b = \Lambda - t/\sin\theta = 222$ nm by air. Electromagnetic plane wave of wavelength λ is incident on the structure at a polar angle θ_{inc}. The spectral-directional reflectance R'_λ is calculated by RCWA algorithm. The grating substrate is considered to be opaque. Hence, absorptance is defined as $\alpha'_\lambda = 1 - R'_\lambda$. As outlined in section 2.3, each Al plate grating is divided into M = 50 rectangular layers to approximate the inclined geometry for RCWA computation. A total of 81 Fourier components are used to

approximate the dielectric function in the grating layer and Al optical constants are taken from tabulated data at room temperature [69].

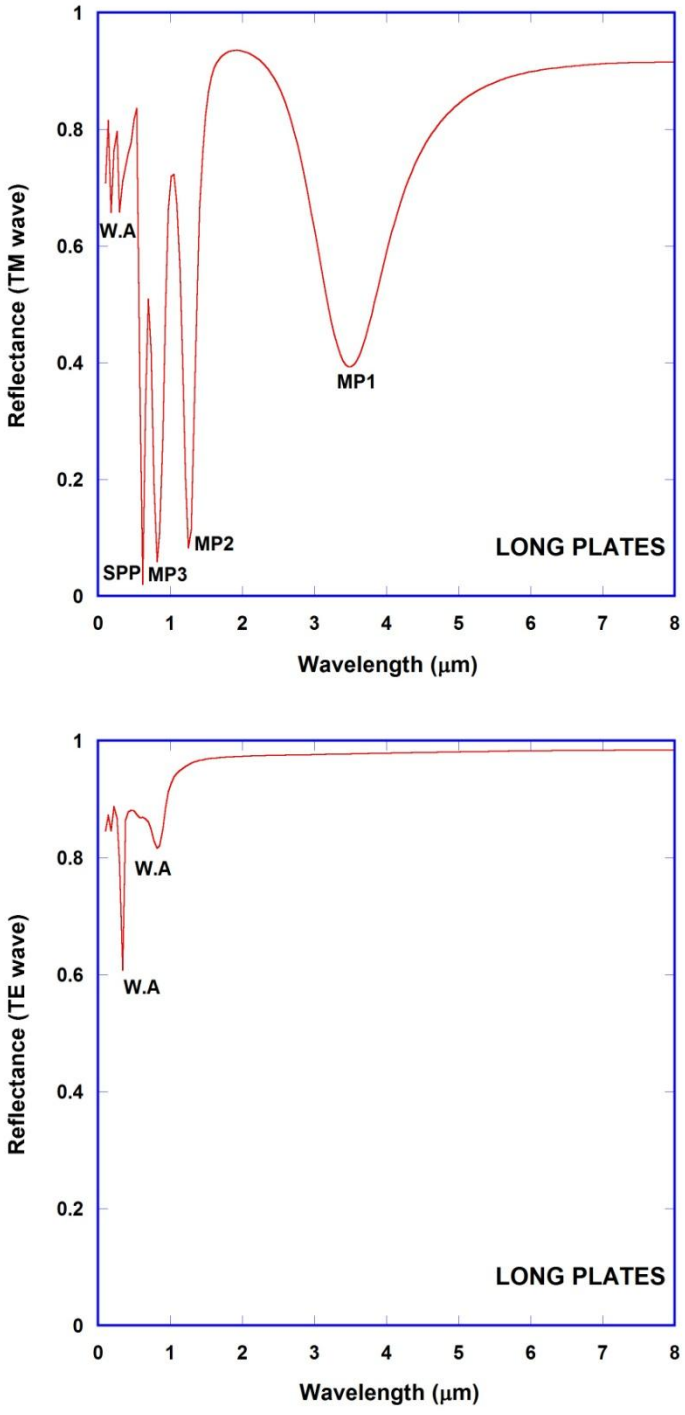

Figure 3.2 TM wave reflectance (at top) and TE wave reflectance (at bottom) of the structure at normal incidence (Long Plates)

Figures 3.2 shows the calculated reflectances of the microstructure at normal incidence, for both TE and TM waves in case of long plates. It is evident from the figures that there exist multiple reflectance dips/absorption peaks for certain wavelengths in case of TM waves, indicating enhanced absorption at these wavelengths. Some of these wavelengths (corresponding to absorption peaks) are at λ = 237 nm, 315 nm, 555 nm, 618 nm, 823 nm, 1.27 μm and 3.55 μm. For TE waves, some of the reflectance dips can be seen at λ = 237 nm, 315 nm and 823 nm. It is to be noted that at λ = 237 nm, 315 nm and 823 nm, both TE and TM waves exhibit reduced reflectance and hence the absorption mechanism here must be independent of polarization. These wavelengths correspond to Wood's anomaly (labeled as W.A in the figure), when a diffracted order reaches grazing angle and the light energy is redistributed when a propagating diffraction order appears. However absorption enhancing wavelengths of 618 nm, 1.27 μm and 3.55 μm are unique only to TM waves, signifying the effect of magnetic resonance at play at these wavelengths. This can be explained by excitation of fundamental and higher order MP modes (excited at higher frequencies or lower wavelengths). Hence, λ = 3.55 μm is the fundamental MP mode (labeled as MP1 in the figure) while λ = 1.27 μm is the second order MP mode (MP2). λ = 618 nm is a possible MP3 which has been coupled with a SPP. Higher order MPs cause a much greater absorption enhancement. MP2 results in roughly 2.3 times more absorption than MP1.

It should also be noted that λ = 555 nm corresponds to increased absorption caused by excitation of SPPs caused by incident photons at Al/air interface (labeled as SPP in the figure). This can be validated by solving the SPP equation given below

$$k_{spp} = \frac{\omega}{c}\sqrt{\frac{\varepsilon_1 \varepsilon_2}{\varepsilon_1 + \varepsilon_2}} \tag{3.1}$$

Here, k_{spp} is the x-component of the wavevector which is a function of both wavelength and incidence angles; ε_1 and ε_2 are the permittivities of air and Al, respectively; ω is frequency of the incident wave and c is the speed of light in vacuum. In case of gratings, the above equation is solved along with the grating equation which allows the dispersion curve to be folded, resulting in SPPs being excited by propagating waves in air. At normal incidence, SPP wavelength is equal to the grating period, as is seen in this case. At oblique incidence, SPP excitation wavelengths can be determined by their dispersion curves.

In case of short plates, TM waves show reflectance dips at λ = 206 nm, 555 nm, 840 nm and 1.26 μm, while TE waves have dips at λ = 206 nm and 840 nm. Please note that the dip at 840 nm for TM wave is not so clear from fig. 3.3 (top) due to low resolution. Once again the dips at λ = 206 nm and 840 nm correspond to Wood's anomaly (W.A) which happens for both TE and TM waves. The dip at λ =555 nm corresponds to SPP absorption which is only dependent on the grating period for normal incidence. Since the grating period for long and short plates is the same, the SPP wavelength remains identical. Increased absorption at λ =1.26 μm is explained by magnetic resonance (MP1). All these features have been labeled in figs. 3.3 below.

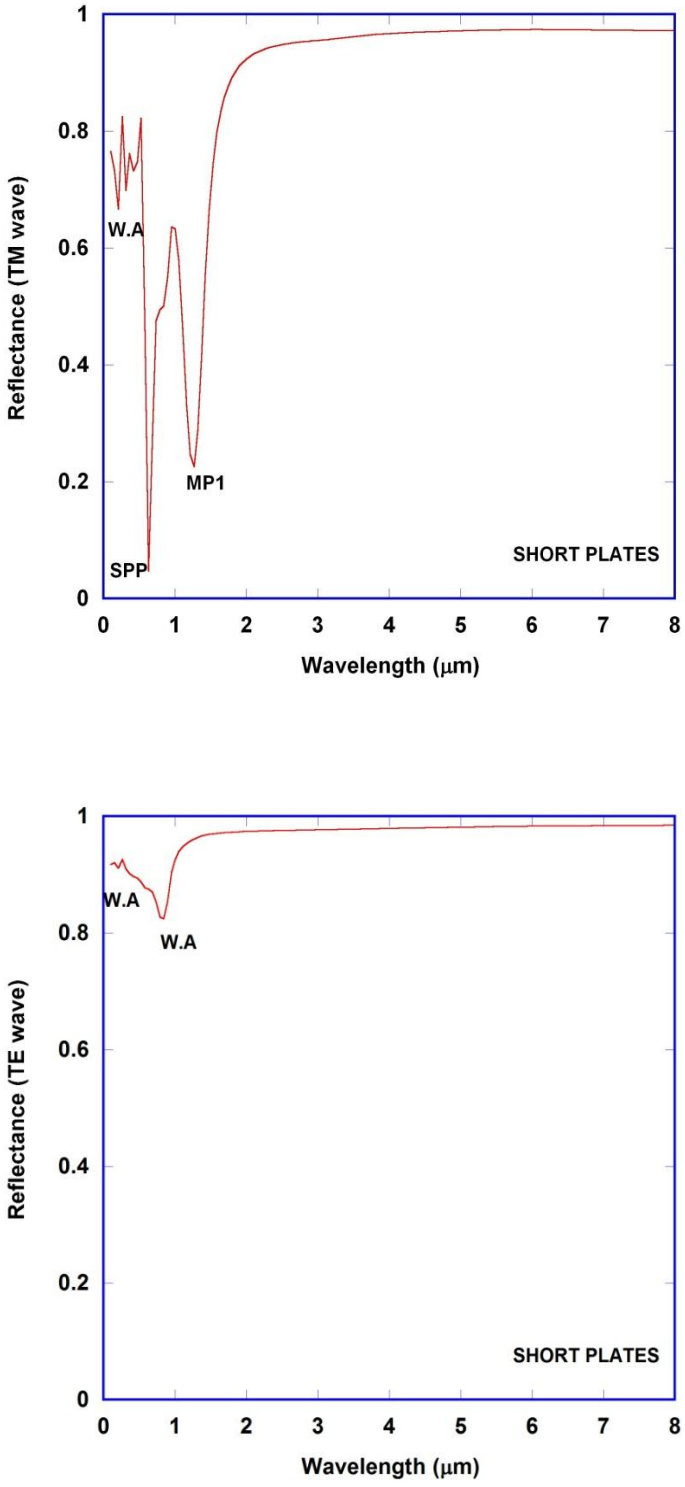

Figure 3.3 TM wave reflectance (at top) and TE wave reflectance (at bottom) of the structure at normal incidence (Short Plates)

The physical mechanism of magnetic polaritons can be explained as follows. According to Maxwell's equations, when a time varying magnetic field is incident perpendicular to the structure (TM waves), it induces an electric current at the surface of the microstructure, which in turn creates an induced magnetic field. When the incident magnetic field and the induced magnetic field are in resonance with each other, then diamagnetic condition is satisfied resulting in strong absorption at particular wavelengths. An important characteristic of magnetic resonance is that induced current forms a loop (antiparallel currents) called an eddy loop according to Lenz's law.

Since we are interested in tailoring radiative properties of microstructures based on resonance behavior of SPPs and MPs which are observed only for TM waves, from now onwards we shall limit our discussion to TM waves only.

3.4.3 Field distribution at magnetic resonance condition

The electromagnetic field distribution for both LP and SP are calculated using RCWA. These field distribution plots help us to understand the field confinement achieved by parallel plate grating array. For LP, field distribution at MP1 and MP2 is plotted at normal incidence and at $\lambda = 3.55\ \mu m$ and $1.27\,\mu m$, respectively in fig. 3.4 (top and bottom). On the other hand, SP has only the fundamental MP resonance mode at $\lambda = 1.26\ \mu m$ whose field distribution is shown at normal incidence in fig. 3.5. The shaded contour represents the logarithm of the square of the ratio of absolute value of magnetic field in the structure to that of the incident wave, and the arrows indicate the electric field directions with their lengths indicating the corresponding amplitudes. The blue colored loops indicate the induced electric currents.

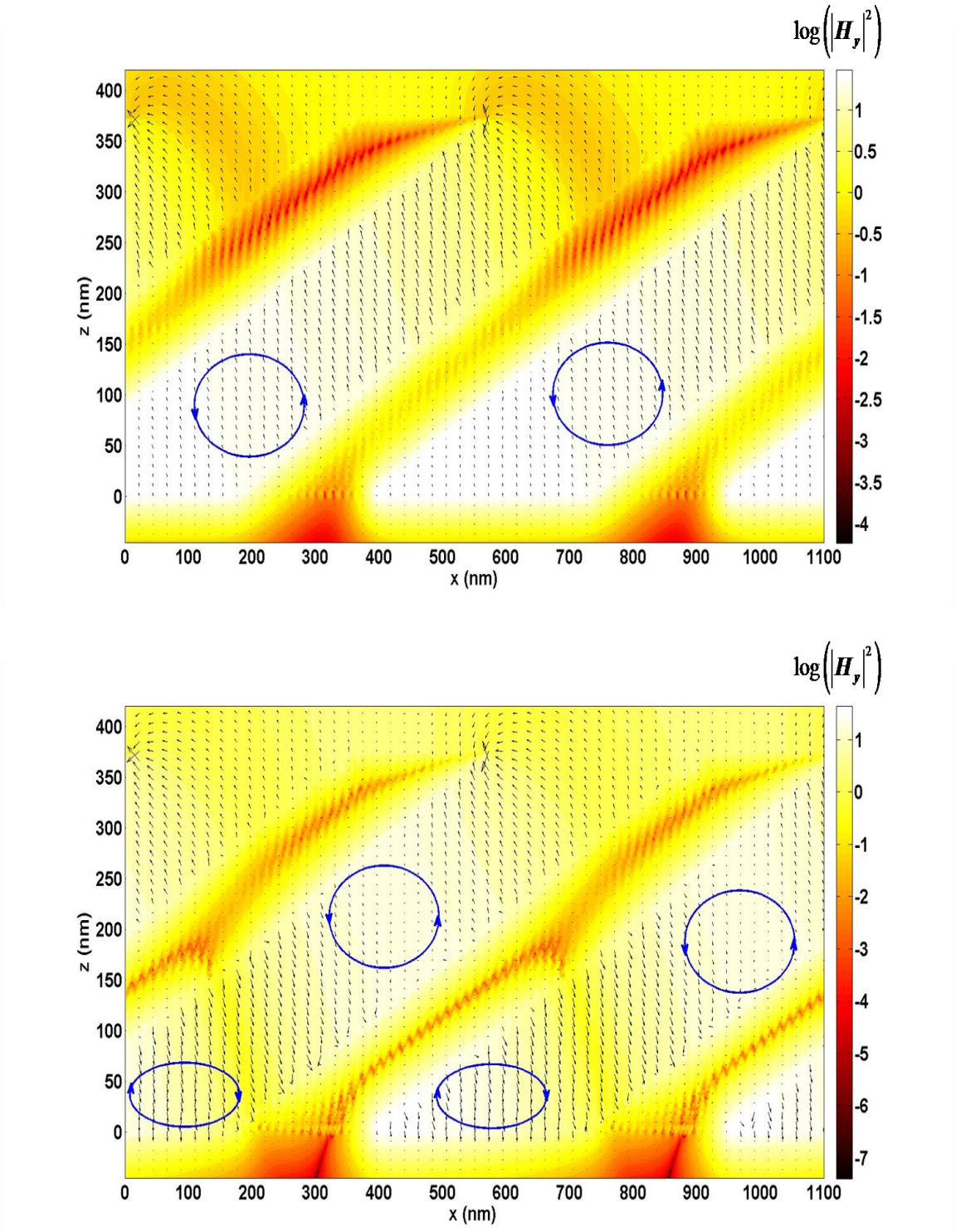

Figure 3.4 Electromagnetic field distribution between long plates at MP1 resonance (at top) and MP2 resonance (at bottom)

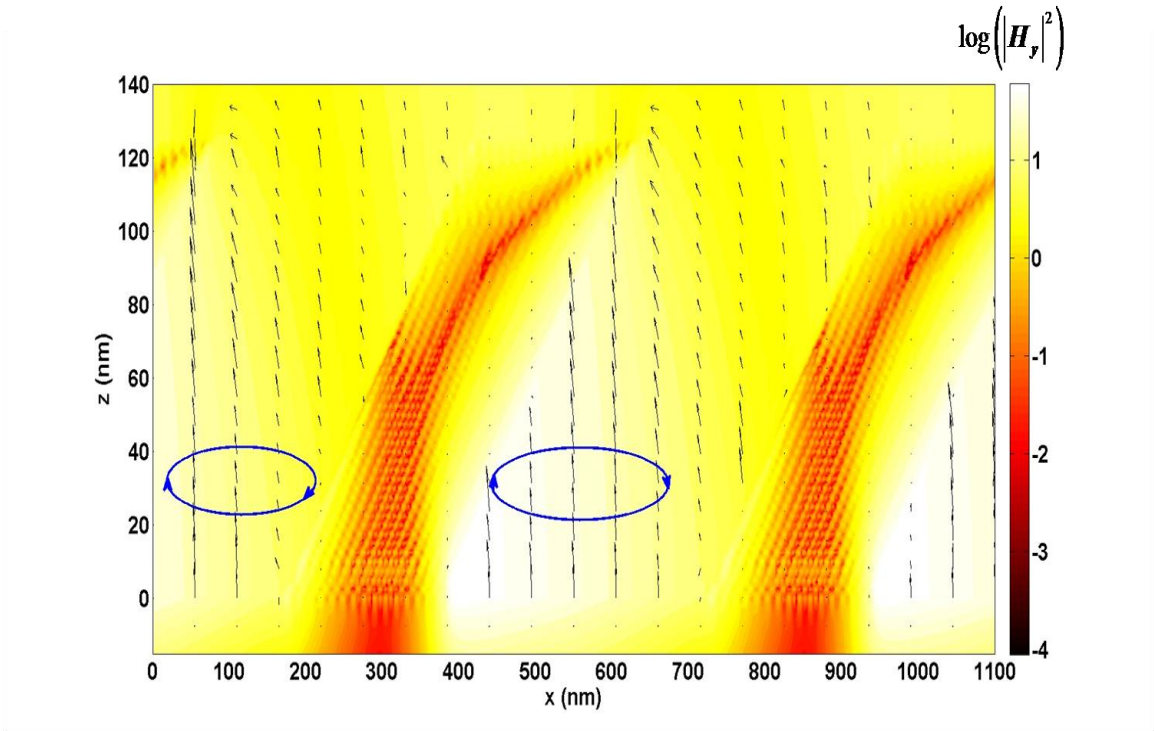

Figure 3.5 Electromagnetic field distribution between short plates at MP1 resonance.

As visible in the above figures, there is strong magnetic field confinement, and hence strong absorption, in the cavity between parallel plates. The electric field vector directions suggest that an eddy current is induced in the structure due to oscillating magnetic fields. Due to formation of eddy currents, positive and negative charges are developed at the two ends of the cavity which suggests that the cavity can be modeled as a capacitor. The eddy current decays rapidly as one moves away from the center of the cavity. Since only one electric field loop is formed in the case for both LP and SP in figs. 3.4 and 3.5, it suggests that magnetic resonance at these wavelengths $\left(\lambda_{LP} = 3.55\ \mu\text{m and } \lambda_{SP} = 1.26\ \mu\text{m}\right)$ is characterized by fundamental mode (MP1). It should be noted that an electric field vector loop is generally formed when antiparallel currents exist in the cavity. However, due the presence of Al substrate, antiparallel

currents cannot be easily visualized. We can still find the direction of the eddy current loop by noting the magnitude of eddy currents (length of electric field vector arrow in the figure) as we move across the entire length of the cavity. The loop in this case is formed by eddy currents flowing from higher electric fields to lower electric fields. Such loops are the ones that are formed in case of MP1 for both SP and LP.

In fig. 3.4 (bottom) for LP, two current loops with alternating directions, corresponding to anti-nodes of magnetic field, are induced in the cavity. This indicates that a second-harmonic MP mode is formed at $\lambda = 1.27\,\mu m$. Due to the presence of 2 magnetic field antinodes, there is much stronger confinement of magnetic field, resulting in much greater absorption for MP2, as compared to MP1. This provides an illustrative proof of the light confinement that occurs between the inclined parallel plate grating array.

3.4.4 Spectral and directional dependence of the radiative properties

The spectral-directional reflectance of these microstructures is shown via two-dimensional contour plots in wavelength-incidence angle (λ-θ_{inc}) coordinate system. Wavelength is plotted along the x-axis while angle of incidence θ_{inc} is along the y-direction. Each plot contains 400 data-points for both λ and θ_{inc}. These contour plots offer a wealth of illustrative information about the effect of different resonance mechanisms such as MPs and SPPs on the radiative properties of parallel plate grating arrays.

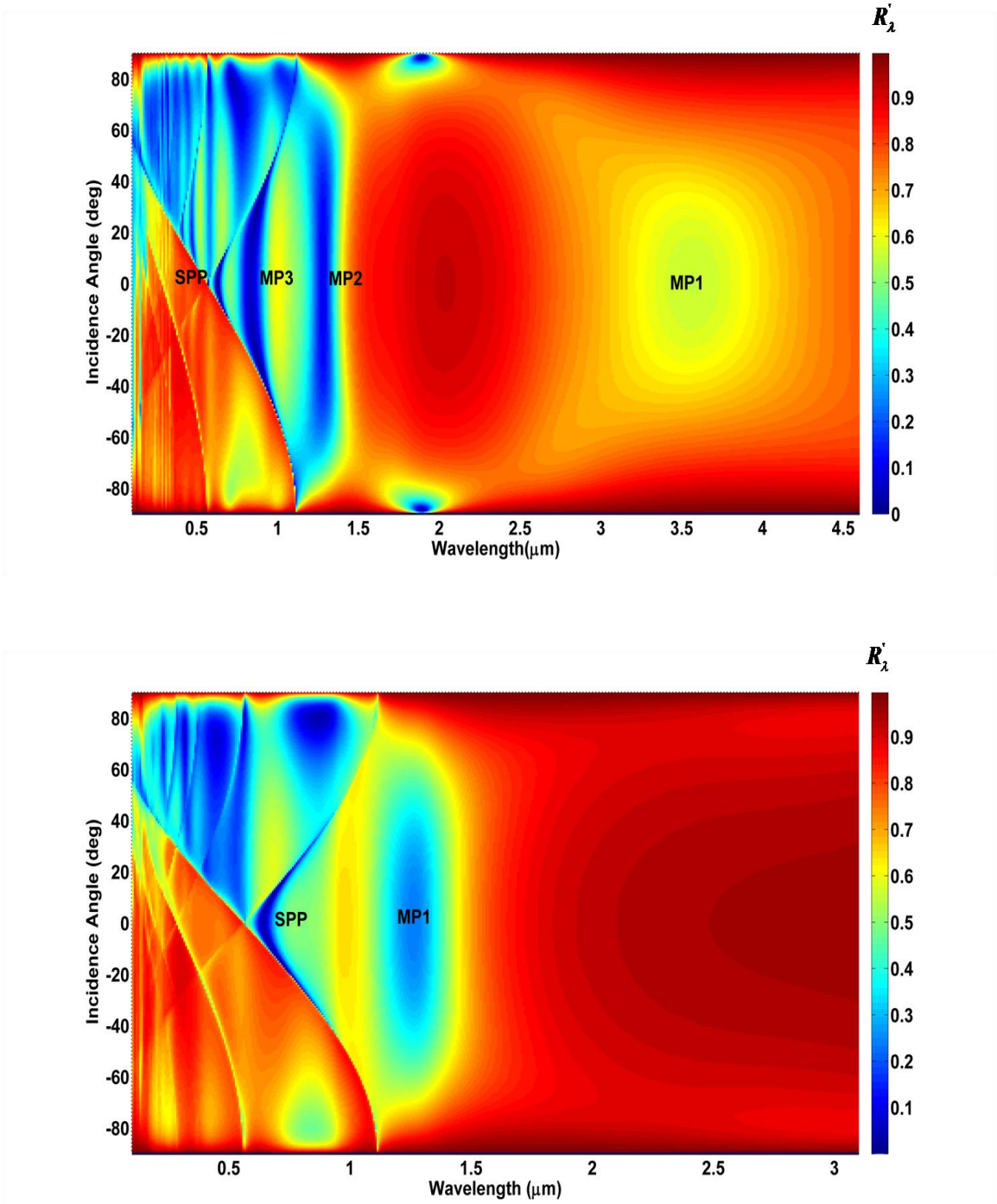

Figure 3.6 Contour plot of spectral-directional reflectance as functions of wavelengths and incidence angles for long plates (at top) and short plates (at bottom)

The SPP dispersion curves, which can be obtained by solving equation (3.1) with the grating equation (2.1), can be seen in the contour plots clearly. These curves are symmetrical with respect to normal incidence. The SPP dispersion curve shown in both the figures are folded at λ = 555 nm due to the same grating period. For LP, the MP modes are shown as MP1, MP2 and MP3 occurring at $\lambda = 3.55\,\mu m$, $1.27\,\mu m$ and 618 nm respectively. For SP, only MP1 is observed at $\lambda = 1.26\,\mu m$. In case of fig. 3.6 (top) for LP, two symmetrical reflectance dips are observed at grazing incidence angles. These could be attributed to high absorption observed in metals at principal angles for TM waves, which occur very close to grazing angles. Another feature to be noted is the non-geometrical optics behavior exhibited by these structures when the wavelength is comparable to the grating period. According to the convention used in this work, a negative angle of incidence implies light is incident on the structure from the right side, where as a positive angle means incident light is coming from the left direction. Since the plates are already inclined towards right, positive incidence implies more light falls directly on Al plates as compared to negative incidence when more light falls on the space between the plates (air). Since Al is a highly reflective metal, higher reflectance for positive incidences and lower for negative incidences is expected from geometric optics. However, the opposite phenomenon is seen through the contour plots, indicating that simple geometrical optics concepts cannot be applied to inclined parallel plate grating arrays when wavelengths are comparable to structural dimensions.

The vertical dispersion curves are a unique feature of MPs, suggesting that magnetic resonance is a weak function of incidence angles. The MPs are effectively excited by the *y*- component of the magnetic field while the *x*-component of the electric

field, which drives the electric dipole oscillation, contributes little to the magnetic resonance. It should also be noted that MP1 provides a more broadband absorption as compared to higher orders such as MP2. This can be utilized in applications where absorption enhancement over a broader spectrum is desired. However, MP2 results in much higher absorption, of up-to 76.5% as compared to 33.8% as achieved in MP1. Since MPs are insensitive to direction, they find use in many applications where SPPs cannot be implemented either because of their directional sensitivity or narrow spectral bands of absorption/reflection. The polar plots, figs. 3.7 and 3.8 included below, show the directional independence of MPs as compared to SPPs for both long and short plates. These plots are calculated at resonance wavelengths of the structure.

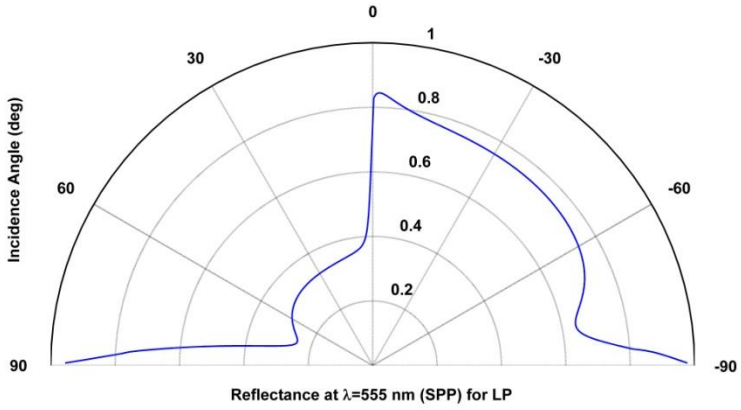

Figure 3.7 Polar plot of reflectance as function of incidence angles for SPP resonance in long plates

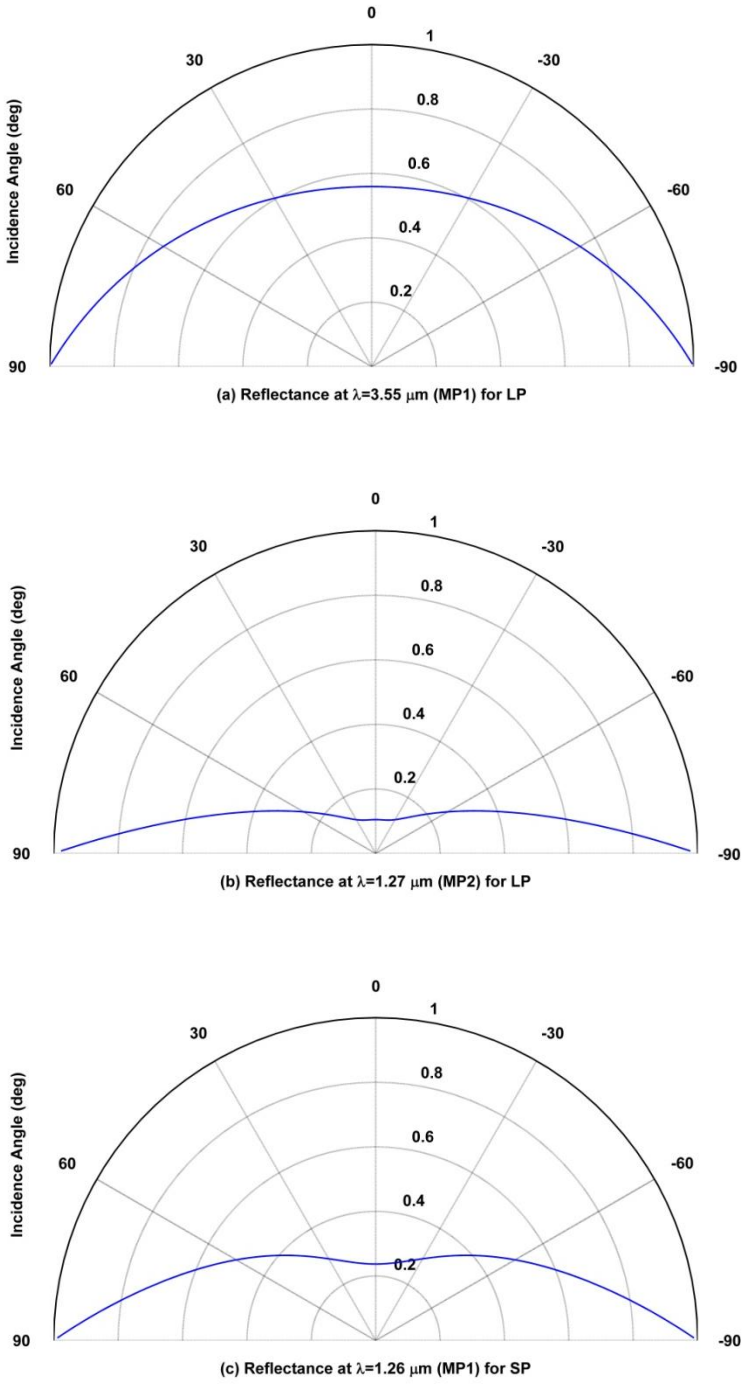

Figure 3.8 Polar plot of reflectance as function of incidence angles for MP1 resonance in long plates (top), MP2 resonance in long plates (centre) and MP1 resonance in short plates (bottom)

From the polar plots above, it can be clearly inferred that MPs have a weak directional dependence whereas SPPs depend strongly on the direction of incoming radiation. One can also see that, on the overall, MP2 for long plates has much lower reflectance as compared to MP1 for either of the plates, a fact which has also been observed from spectral-directional contour plots. MPs not only are symmetrical with respect to normal incidence, but also have a relatively uniform reflectance for oblique incidence angles, signifying their directional and hemispherical independence. On the other hand, SPPs have an unsymmetrical reflectance profile with respect to normal incidence and a very strong dependence on incidence angles for oblique incidences.

3.4.5 LC circuit model

The LC circuit model provides quantitative evidence of the existence of fundamental MP mode (MP1) present in the structure [70]. It analytically predicts the magnetic resonance frequency based on impedance analysis of structures composed of equivalent inductances and capacitances. Figure 3.9 shows the equivalent LC circuit of the grating structure. For periodic structures, each plate (or groove) can be considered as an isolated unit as long as the thickness of the plates is much greater than radiation penetration depth, which is true in our case.

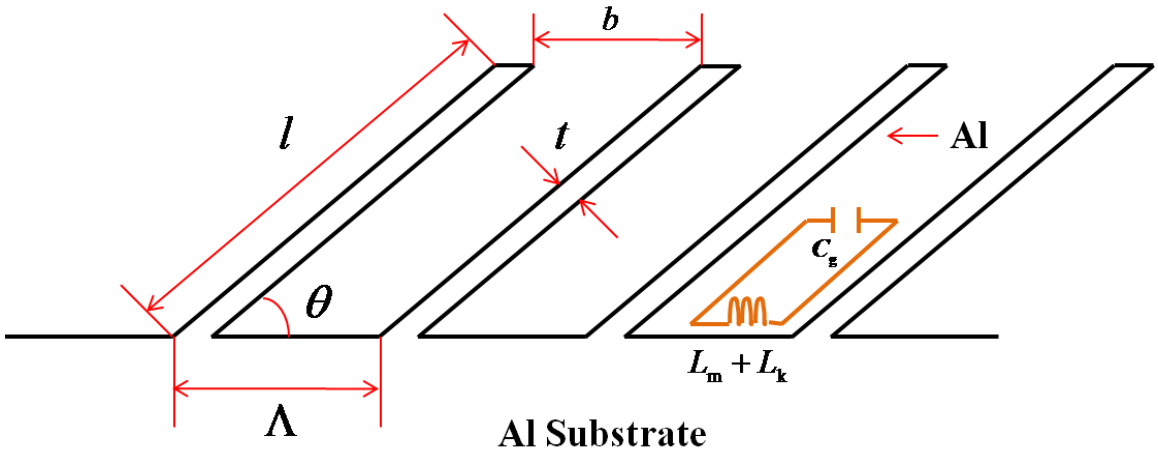

Figure 3.9 Two-dimensional view of the grating array showing the LC circuit model as inset

The whole circuit is composed of two inductances and one capacitance. L_m is the magnetic inductance of the two parallel plates separated by distance $b = \Lambda - t/\sin\theta$, based on the coil inductance. It is expressed as

$$L_m = \frac{\mu_0 b l \sin\theta}{w} \tag{3.2}$$

Here μ_0 is the magnetic permeability in free vacuum; w is the plate width along the y-direction. For metallic nanoscale structures, the contribution of drifting electrons to the inductance (called the kinetic inductance) should also be taken into account as

$$L_k = \frac{s}{\omega_p^2 \varepsilon_0 A_{eff}} \tag{3.3}$$

where $s = (2l + b)$ is the distance the induced current circulates in the open loop; $\omega_p = 2.4 \times 10^{16}$ rad/s is the plasma frequency of Al [3] ; A_{eff} is the effective cross-sectional area for the induced current due to skin effect and non-uniform charge distribution and ω

is frequency of the incident wave. By assuming that the flow of induced current is approximately limited to a depth equal to the skin penetration depth $\delta = \lambda / (4\pi\kappa)$ [3] we can take the effective cross sectional area to be $A_{\text{eff}} = \delta w$. After including some other approximations, eq. (2.27) can be rewritten as

$$L_{\text{k}} = \frac{(2l + b)}{\omega_{\text{p}}^2 \varepsilon_0 \delta w} \tag{3.4}$$

The air gap between successive parallel plates is modeled by a gap capacitance C_{g} whose magnitude is given by

$$C_{\text{g}} = \frac{c_1 \varepsilon_0 A_{\text{proj}}}{d_{\text{proj}}} \tag{3.5}$$

In the case of inclined parallel plates, projected areas and distances are calculated as $A_{\text{proj}} = \left(l - b/\cos\theta\right) w$ and $d_{\text{proj}} = b \sin\theta$, respectively. The factor c_1 is introduced to include the non-uniform charge distribution between the parallel plates. It is difficult to determine the exact value of c_1 without knowing the exact charge distribution. Here c_1 is chosen to be 0.50. It should be noted that the magnetic resonance conditions are independent of plate width in the *y*-direction, w.

The total complex impedance of the LC circuit is then given by

$$Z_{\text{tot}} = i\omega \left(L_{\text{m}} + L_{\text{k}} - \frac{1}{\omega^2 C_{\text{g}}} \right) \tag{3.6}$$

where $i = \sqrt{-1}$ is the unit imaginary quantity. Magnetic resonance for the fundamental mode of MPs is achieved when the total impedance $Z_{\text{tot}} = 0$. This enables us to find the

resonant frequency $\omega_{R,1}$, and hence resonance wavelength $\lambda_{R,1}$, for the fundamental mode of MPs, corresponding to a low reflectance value which is given by

$$\lambda_{R,1} = 2\pi c\sqrt{(L_m + L_k)C_g} \tag{3.7}$$

Based on Eq. (3.7), the resonance wavelength of MP1 for LP is predicted to be $\lambda_{R,1}$= 3.44 μm, which has a relative difference of 3.1% from the RCWA calculations. Considering the approximations made with regard to c_1 and A_{eff}, this agreement is reasonable. Further comparisons are made between LC circuit model and RCWA calculations by varying different geometric parameters, as discussed in the section below.

3.5 Geometric Effects on Magnetic Resonance

The geometric effects on the magnetic resonance conditions are studied by individually changing plate length(l), thickness(t), period(Λ), and inclination angle (θ), keeping the LP configuration parameters as base values. Note that LC circuit model only predicts MP1 resonance condition; hence only MP1 calculations are compared between RCWA and LC circuit model. The spectral-directional contour plots show the reflectance at normal incidence calculated from RCWA method. All the plots consist of 400×400 data points of wavelength and a relevant geometrical parameter. The predicted $\lambda_{R,1}$'s from LC circuit model is shown as a filled black colored triangles.

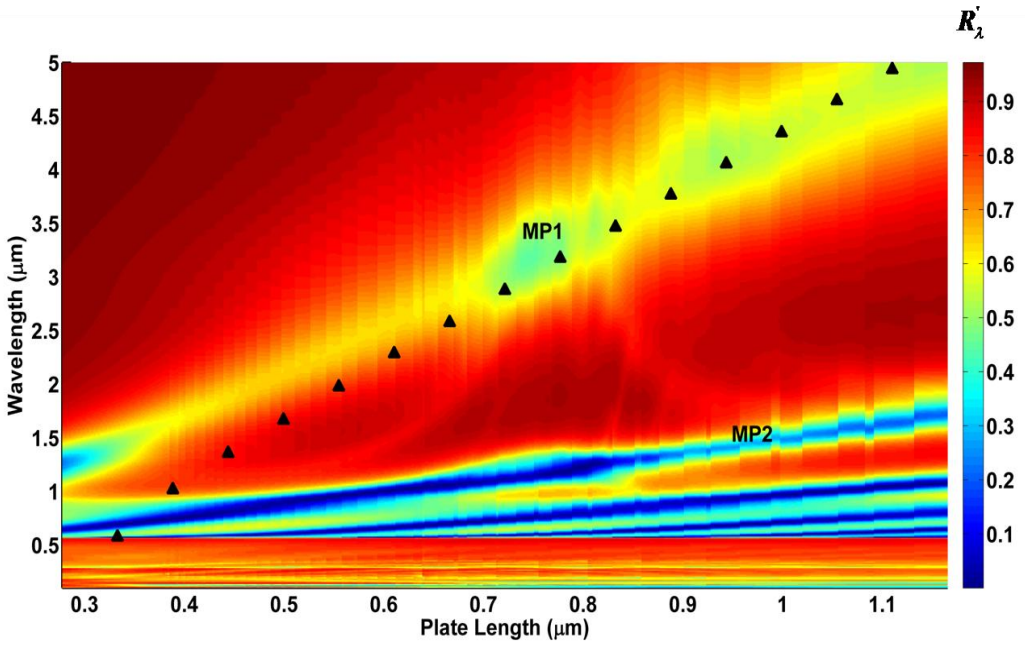

Figure 3.10 Effect of varying plate length *l* on magnetic resonance of the considered microstructures through spectral-directional contour plot of reflectance at normal incidence.

In fig. 3.10, the effect of plate length on MP1 resonance conditions is investigated. For the RCWA calculations, plate length is varied from 0.1 μm to 1.15 μm, while wavelength is varied from 0.1 μm to 5 μm. From the contour plot, it is clear that increasing the plate length causes the MP1 resonance wavelength to increase as well, which agrees with the prediction from LC circuit model. L_k, L_m and C_g increase or decrease with a corresponding increase or decrease in plate length, and hence according to Eq. (3.7), an increase in plate length does correspond to an increase in resonant wavelength. As the plate length decreases, the agreement is not so good which can be explained by the fact that MP1 resonance becomes coupled to SPP resonance at these plate lengths, and LC circuit model does not take coupling into account.

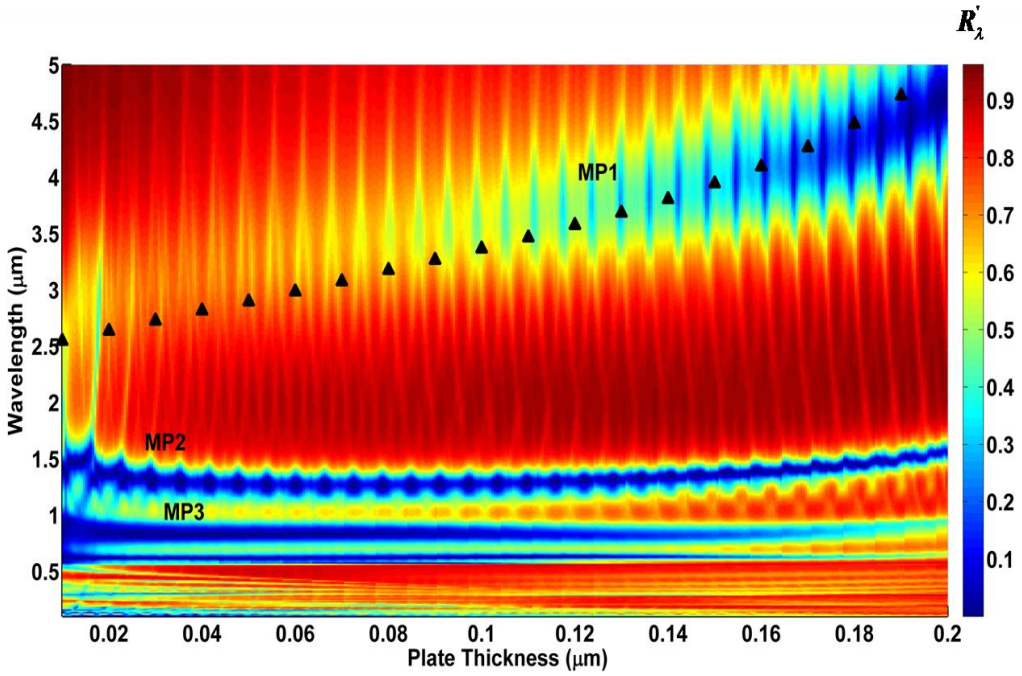

Figure 3.11 Effect of varying plate thickness *t*, on magnetic resonance of the considered microstructures through spectral-directional contour plot of reflectance at normal incidence.

In fig. 3.11, plate thickness is varied from 0.01 μm to 0.2 μm while wavelength range is kept the same as in the previous case. From the RCWA calculations, it can be seen that an increase in plate thickness increases the resonance wavelength of MP1, a phenomenon that be clearly verified by the LC circuit model. The agreement between LC circuit model and RCWA calculations is very good over the range of plate thicknesses considered, with discrepancies cropping up for thin plates. As *t* increases, *b* decreases resulting in a corresponding decrease in L_m, L_k and increase in C_g. The increase in C_g may be able to compensate for the decrease in L_m and L_k, resulting in higher resonant wavelengths for thicker plates. The LC model may not be applicable for thin plates since

the neighboring cells do not remain uncoupled any more. There are two other interesting points that are worth noting. Firstly, on close scrutiny we can see that as the order of MPs increase, they become more independent of plate thicknesses. Thus MP3 is a much more flat curve compared to MP2 which is flatter than MP1. The second observation is that, for MP1 and, to a certain extent, for MP2, the strength of resonance increases with thickness with extremely strong absorption occurring for values of *t* greater than 175 nm. This phenomenon is not so clear in higher order harmonics. Put together, these 2 facts may be utilized to design directionally independent microstructures with high absorption.

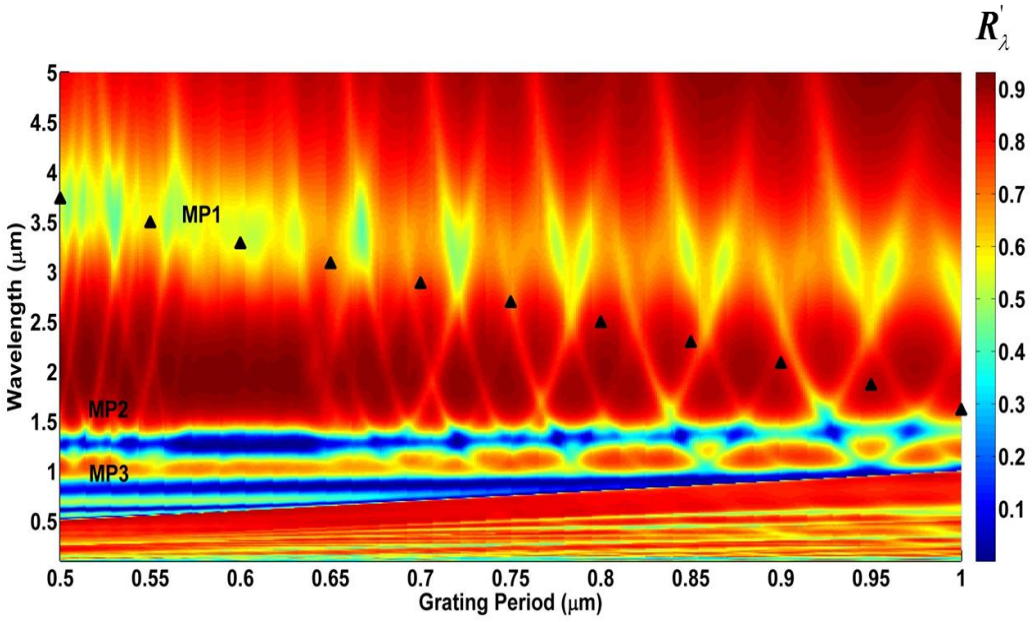

Figure 3.12 Effect of varying grating period Λ on magnetic resonance of the considered microstructures through spectral-directional contour plot of reflectance at normal incidence.

Fig. 3.12 shows the effect of varying grating period on MP1 resonance conditions. The period is varied from $0.5\,\mu m$ to $1.0\,\mu m$. As the grating period increases, the resonance frequency increases as well, resulting in decrease of resonant wavelength. The

RCWA agreement with LC circuit model decreases appreciably as the grating period increases i.e. the successive plates are farther apart. The reasons could that at higher periods, the MP resonance modes tend to become coupled to each other or the capacitor model may have larger error which becomes amplified with increase in period.

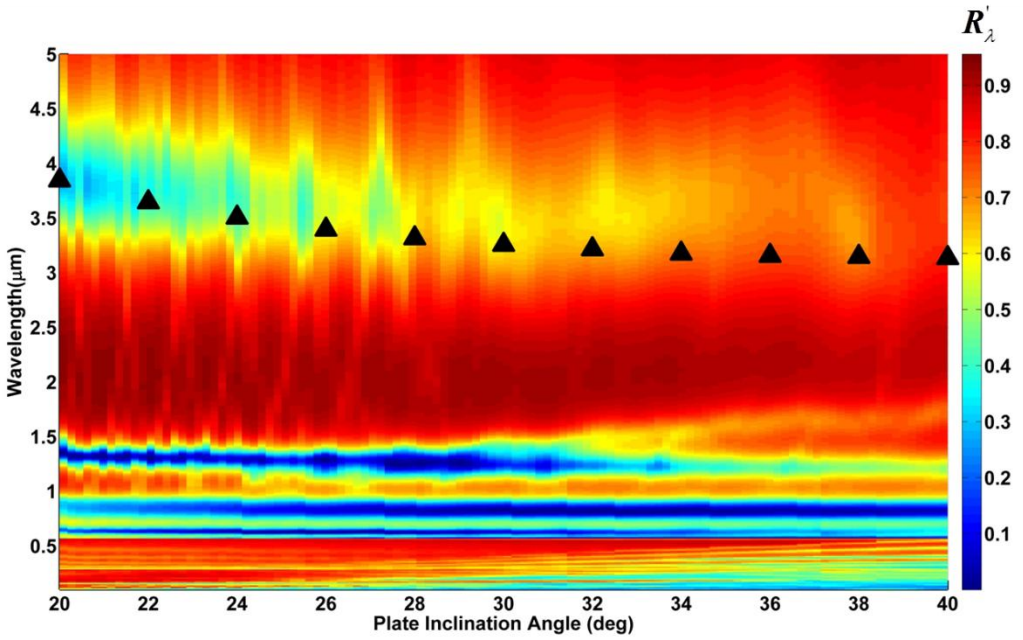

Figure 3.13 Effect of varying plate inclination angle θ on magnetic resonance of the considered microstructures through spectral-directional contour plot of reflectance at normal incidence.

Finally the effect of variation of plate inclination angle θ on MP1 resonance conditions is studied in fig. 3.13. Upper limit of θ has been fixed at 40 degrees, because MP1 resonance starts fading beyond this value. RCWA calculations predict a slight decrease in MP1 resonance wavelength with increase in θ, which is confirmed by the LC circuit model as well. Variation in b can be assumed to be negligible in the given θ range. The agreement is quite good for shorter plate inclination angles. At higher values

of θ, it is difficult to quantify the level of agreement between the numerical and analytical approaches because MP1 resonance starts fading very fast for θ beyond 35 degrees.

3.6 Conclusion

This chapter discusses the various mechanisms responsible for causing enhanced absorption in inclined parallel plate grating arrays. Wood's anomaly, SPP and MP resonances are discussed with regard to both long and short plate lengths. Visual evidence for SPP and MP is provided through electromagnetic field distribution plots, spectral-directional contour plots and polar plots in the case of TM waves which are computed using RCWA. Analytical agreement with visual data is obtained through use of LC circuit model which provides an approximate value of the MP1 resonance frequency. Finally a parametric study is conducted to investigate the effect of different geometric parameters on the resonance wavelength of MP, through the use of RCWA method and further confirmed by application of LC circuit model. A better understanding of the various resonance mechanisms and geometrical parameters responsible for enhancing grating absorption will facilitate design of microstructures which are optimally suited for energy harvesting and sensing applications.

CHAPTER 4

APPLICATION OF RCWA TO STUDY OF SILVER NANORODS ON COMPACT DISC GRATINGS

4.1 Introduction

Owing to their unique and tunable optical, plasmonic, and electrical properties, silver nanorods are widely used for applications such as SERS, biological sensors, and chemical detectors [4, 6]. Arrays of AgNRs are considered as prospective structures for near field transmission [71] and can be modified to enable subwavelength imaging of arbitrary coherent sources [72]. AgNR arrays have been previously used to create surface plasmon resonance sensors which are valuable tools for investigating chemical and biological events on surfaces [5]. Their SERS properties have also been exploited to create structures which can provide structural and quantitative information about biological virus strains through spectroscopic characterization [73]. Because of their immense use in life sciences related applications, experimental and theoretical studies to characterize their radiative properties are considered to be of crucial importance. This chapter aims at the characterization of radiative properties of AgNR arrays obliquely aligned on a grating layer.

4.2 Fabrication of Silver Nanorod Samples

The AgNRs are fabricated by an oblique angle deposition (OAD) method [4], which is a physical vapor deposition method with advantages of high yield, low cost and excellent geometry control. The deposition occurs in a custom designed electron-

beam/sputtering evaporation chamber. The growth substrate is a CD which is 150 mm in diameter with a grating period of 1.5 μm. On top of the CD, there is a thin uniform gold (Au) film with a thickness of 0.05 μm. The CD is positioned directly above the Ag evaporation source and rotated at an angle of 86 degrees with respect to the deposition vapor incoming direction. As the source evaporates, Ag is deposited on the CD surface in the form of nanorods which tilt downwards towards the incident vapor direction, making an angle of β=70 degrees with the CD normal. Two samples are cut from the CD substrate at the locations shown in the figure below. Sample 1 is cut in the vertical direction with AgNRs perpendicular to the CD grooves and sample 2 is cut in the horizontal direction with AgNRs parallel to the CD grooves. Depending on the location where the AgNRs are deposited on the CD, the AgNR projection of sample 1 is perpendicular to the CD grooves and that of sample 2 is parallel to the CD grooves. For sample 1, which is located directly above the source, AgNR distribution is relatively uniform in the CD ridges and grooves while for sample 2, which is not directly above the source, AgNR growth exhibits a strong radial dependence. This results in non-uniform deposition along CD ridges and grooves due to shadows cast by ridges on grooves. Based on Scanning Electron Microscope (SEM) images, the average length and diameter, statistically estimated over 50 rods, are approximately l = 1.2 μm and d = 0.1 μm, respectively. The volume filling fraction of AgNRs is also estimated to be ϕ = 0.4. Fabrication of these samples was done in Dr. Yiping Zhao's group at the University of Georgia. We have performed both experimental and theoretical studies on the diffraction behavior of AgNR to study their radiative properties. SEM images of the samples are shown in fig. 4.1 below.

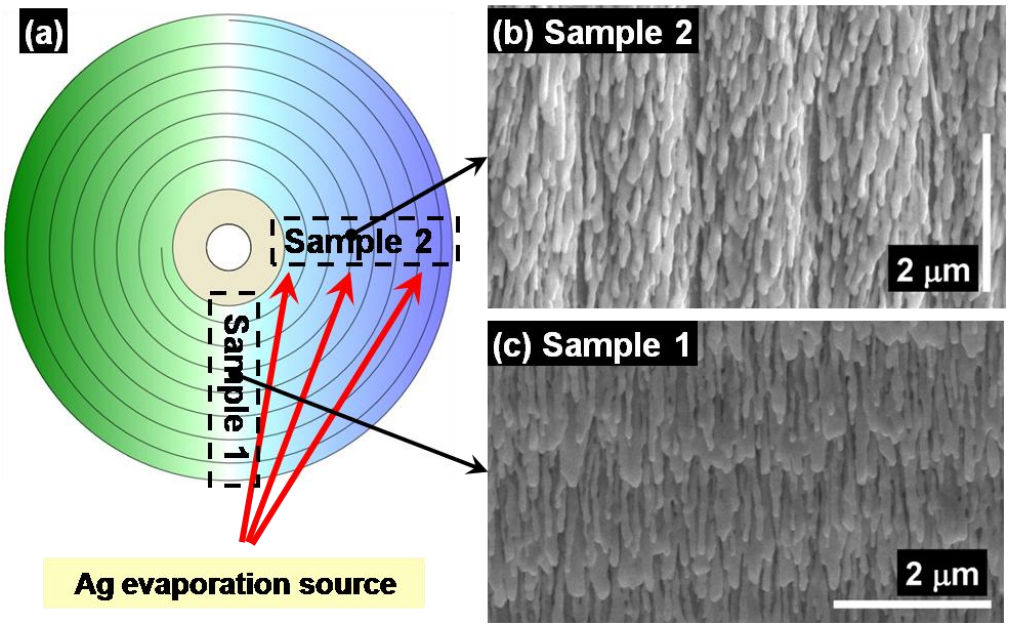

Figure 4.1 SEM images of the sample: (a) locations of Samples 1 and 2 on the whole CD wafer, Samples 1 and 2 are cut along the vertical and horizontal directions, respectively; (b) SEM image taken at the center of Sample 2 with AgNRs parallel to CD grooves; (c) SEM image taken at the center of Sample 1 with AgNRs perpendicular to CD grooves

4.3 Experimental Setup for Diffraction Measurement of AgNRs

4.3.1 Three-axis automated scatterometer

The instrument used to observe and quantify the diffraction phenomenon is a three-axis automated scatterometer (TAAS) [3, 74] setup at 635 nm wavelength. The TAAS is used to measure the bidirectional reflectance distribution function (BRDF) of rough surfaces and is capable of both in-plane and out-of-plane measurements. The estimated combined measurement uncertainty is 0.5% at θ_r=45 degrees and 2% at θ_r=80

degrees, where θ_r is the angle of reflection. This does not consider the effect of stray light and misalignments.

The BRDF is a material property that used to characterize the reflection features of a surface. It is essential for many applications in optical and thermal engineering, such as temperature measurement of silicon wafers in a rapid thermal processing furnace [75-77]. BRDF depends on the surface properties (such as refractive index) as well incident light parameters. It is defined as [3]

$$f_r(\theta_i, \varphi_i, \theta_r, \varphi_r) = \frac{dL_r(\theta_i, \varphi_i, \theta_r, \varphi_r)}{L_i(\theta_i, \varphi_i)\cos\theta_i d\omega_i} (\text{sr}^{-1}), \tag{4.1}$$

where (θ_i, φ_i) and (θ_r, φ_r) denote the incidence and reflection directions, respectively, L_i is the incident radiance within an elemental solid angle $d\omega_i$ and dL_r is reflected radiance. The product of L_i and $\cos\theta_i d\omega_i$ is called incident irradiance and has the unit of flux.

The instrument consists of the following major components: an optical source, a goniometric table, and detection and data acquisition systems. The optical source is a fiber-coupled laser diode which provides nearly collimated, coherent and unpolarized light of wavelength 635 nm. The diode exhibits excellent power stability and monochromaticity with the full width at half maximum (FWHM) of the spectral peak to be less than 2 nm. The light passes through a linear polarizer which alters the polarization state of the beam to either TE or TM wave. The polarizer is followed by a beamsplitter which splits the incident light into 2 signals of unequal magnitudes. A labeled image as well as a schematic of the entire setup is shown in figures 4.2 (a) and (b), respectively.

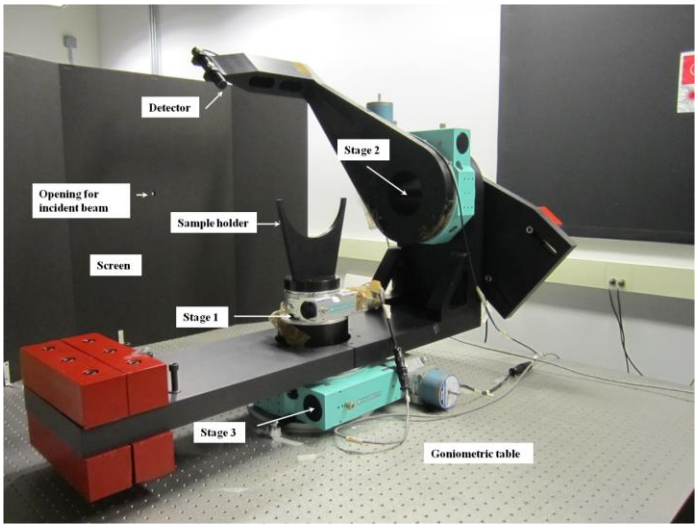

(a)

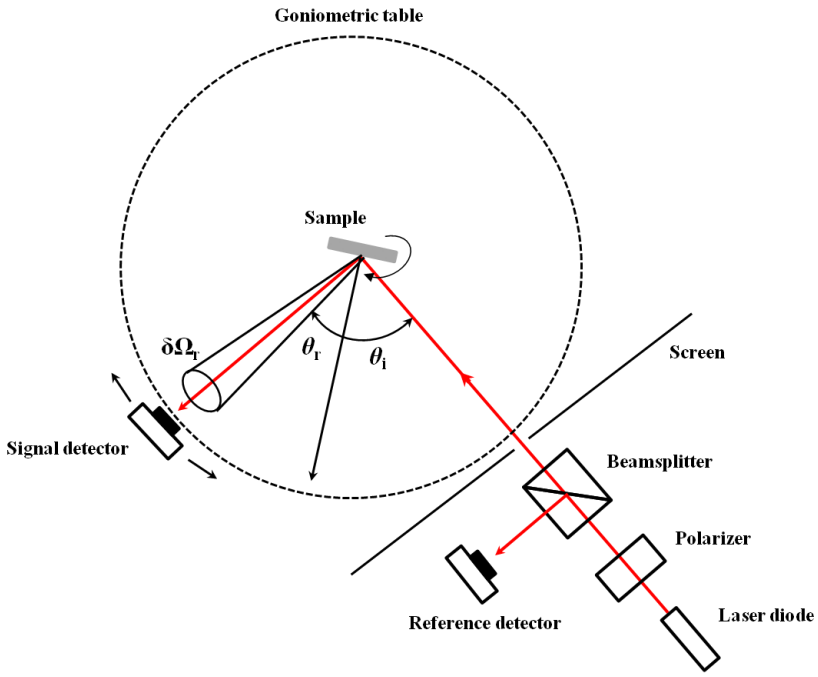

(b)

Figure 4.2 (a) Setup and (b) Schematic of three-axis automated scatterometer for BRDF measurements

The TAAS consists of 3 stages capable of independent rotation which are attached to the goniometric table. Each stage rotation is controlled by step motors, which provides a high degree of resolution and repeatability. The sample is mounted in a vertical holder such that it is perpendicular to the table. Stage 1 controls the incidence polar angle of the sample. Stages 2 and 3 are responsible for controlling the movement of the detector. Stage 2 varies the reflection polar angle of the sample and Stage 3 changes the azimuthal angle. The zero position for the rotary stages correspond the normal incidence/reflection in the sample coordinate which is introduced in section 4.5.

Two silicon photodiode detectors are used for signal collection: detector A measures the signal reflected by the sample and detector B measures the reference signal reflected by a beamsplitter. The detector solid angle for both detectors is $\delta\omega_{\mathrm{r}} = 1.84\times10^{-4}$ sr resulting in half cone angle of 0.45 degrees. Two preamplifiers magnify the magnitude of the low power signals and a lock-in amplifier automatically phase locks the two detector signals at 400 Hz with respect to the internal reference of the amplifier for modulation of the laser source. LABVIEW program on a computer attached to the TAAS system is used to control stage rotation as well as perform automatic data acquisition. Spectral-directional reflectance is calculated by the following formula [3]

$$R_{\lambda}^{'} = \int_{2\pi} f_{\mathrm{r}} \cos\theta_{\mathrm{r}} \delta\omega_{\mathrm{r}}, \tag{4.2}$$

where BRDF related to measured quantities is given by [3]

$$f_{\mathrm{r}}\left(\theta_{\mathrm{i}},\varphi_{\mathrm{i}},\theta_{\mathrm{r}},\varphi_{\mathrm{r}}\right) = C_{\mathrm{I}} \frac{V_{\mathrm{A}}}{V_{\mathrm{B}} \cos\theta_{\mathrm{r}} \delta\omega_{\mathrm{r}}} \tag{4.3}$$

V_A and V_B are the signals received by detectors A and B, respectively and C_I is a compensating factor accounting for beamsplitter ratio and the different responsivities of the two detectors.

4.3.2 Integrating sphere system

The integrating sphere (IS) system is used to measure the directional-hemispherical reflectance (DHR) of both samples [78]. The setup consists of a light source, a monochromator and the integrating sphere. Incident light from a tungsten halogen lamp source is allowed to pass through the monochromator at selected wavelengths. The output signal from the monochromator is modulated by a mechanical chopper to achieve a high signal-to-noise ratio. The integrating sphere, 200 mm in diameter, has its inner wall coated by Polytetrafluoroethylene (PTFE). Both the entrance and exit port diameters are 25 mm. For reflectance measurements, the sample is placed behind the backport of the sphere and detector is placed at bottom of the sphere below a baffle shielding. LABVIEW program controls data acquisition and wavelength selection.

4.4 Diffraction Measurements

Only the diffraction peaks are captured in TAAS measurement, and scattered components are not measured. Eq. (4.2) is used to calculate the peak reflectance, or diffraction efficiency, for each order. It should be noted that at normal incidence, 0^{th} order ($m = 0$) diffraction peak cannot be observed because the incident wave is blocked by the detector and hence an incidence angle of -4 degrees is used to capture this peak. The IS is used to measure the DHR of both samples for each polarization. Table 4.1

shows the individual reflectance of each diffraction order measured by TAAS as well as DHR values for each sample and polarization.

Table 4.1 Measured values of individual reflectance as well as total reflectance for both polarizations for sample 1 and sample 2

Sample #	**Polarization**	**Diffraction Order**					
		$m=-2$	$m=-1$	$m=0$	$m=1$	$m=2$	DHR
Sample 1	TE	0.0006	0.0028	0.0291	0.063	0.0076	0.577
	TM	0.001	0.0173	0.287	0.287	0.032	0.876
Sample 2	TE	0.017	0.232	0.105	0.111	0.015	0.870
	TM	0.003	0.025	0.013	0.010	0.005	0.463

4.5 Sample Geometry and Orientation

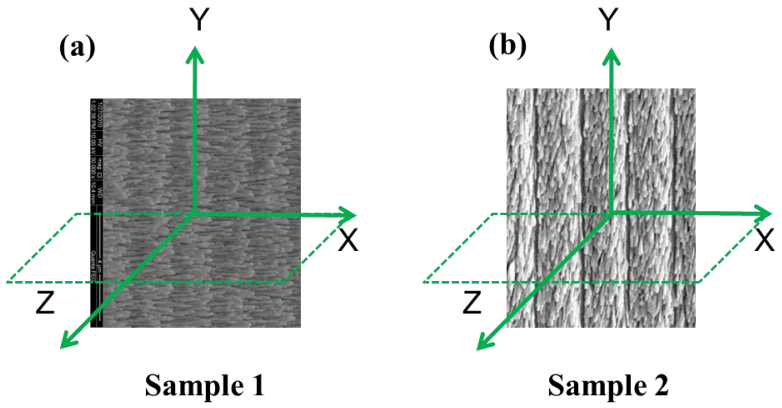

Figure 4.3 Front views of (a) sample 1 and (b) sample 2, showing the orientation of AgNRs with respect to the defined *XYZ* coordinate system. The grating grooves are along Y direction and the dotted *X-Z* plane is the plane of incidence.

The sample is loaded in the *X*-*Y* plane such that the CD grooves are along the positive *Y* direction. The AgNRs are inclined towards the incident vapor direction and hence as such, they are in positive *X* direction for sample 1 and along the negative *Y* direction for sample 2. Light is incident at near normal angles (θ_i = -4 degrees) on the CD grooves such that the *X*-*Z* plane is the plane of incidence. Based on this convention, positive diffraction orders are along negative *X* direction and negative diffraction orders are along positive *X* direction. When the incident magnetic field vector $\mathbf{H}$ is perpendicular to the optical axis of AgNR (denoted by $\hat{\mathbf{c}}$), the incident wave is denoted as an extraordinary wave. Correspondingly, when incident electric field $\mathbf{E}$ is perpendicular to $\hat{\mathbf{c}}$, the incident wave is called as ordinary wave. Hence, a TE polarized wave incident on sample 1 (or TM polarized wave on sample 2), results in an ordinary wave effect (dielectric behavior) and incident TM polarization on sample 1(or TE polarization on sample 2) results in extraordinary wave effect (metallic behavior). Note that bold face implies a vector quantity. Figure 4.3 above graphically describes the above mentioned geometry and orientation graphically.

4.6 Calculation of Optical Constants

The optical constants and dielectric function of AgNRs are calculated using the Drude model [3] of bulk silver with modified parameters. The Drude model used in this study has a scattering rate of $\gamma = 2.7 \times 10^{13}$ rad/s, plasma frequency of $\omega_p = 1.39 \times 10^{16}$ rad/s and ε_∞ =3.4 [68]. To take into account the enhanced scattering rate due to size effect of AgNRs as compared to bulk silver, γ is multiplied by a factor of 10. The dielectric constants silver (Ag) [69].

4.6.1 Effective medium theory

Before proceeding to rigorous coupled-wave analysis of the samples, we need to determine the optical constants of the AgNR-air layer. Based on the SEM images of the sample, filling fraction for the nanorods is approximated as $\phi = 0.4$. The rest of the space between nanorods is filled with air. We may approximate the composite layer made of air interspersed with AgNRs as an effectively homogenous layer, and model its optical constants using the Effective Medium Theory (EMT). EMT is a homogenization method used to characterize the optical properties of inhomogeneous media based on the field average [79]. Theoretical formulations by Maxwell-Garnett (MG) and Bruggeman (BG) are the two widely used approaches used in EMT. MG applies to particles which are embedded in a host (hence is valid for small filling fraction of the particles), while BG assumes structural equivalence between host and the embedded particles (hence is valid for relatively high filling fraction of particles). In our case, Ag rods are assumed to be the embedded particles and air to be the host. Although the filling fraction of AgNR array is not that small, but since they have very good alignment we use the MG approach in our calculations. Also due to the high-aspect ratio of the rods, the array can be considered as uniaxial medium [80]. Hence, their dielectric function can be divided into two components: ε_{O} and ε_{E} corresponding to dielectric functions for ordinary and extraordinary waves, respectively. The relation between **E** and $\hat{\mathbf{c}}$ for ordinary waves and **H** and $\hat{\mathbf{c}}$ extraordinary waves is outlined in section 4.4. Based on MG theory, effective dielectric function for the composite layer is given by the following equation

$$\frac{\varepsilon_k - \varepsilon_{\mathrm{air}}}{\varepsilon_{\mathrm{air}} + L_k(\varepsilon_k - \varepsilon_{\mathrm{air}})} = \phi\left(\frac{\varepsilon_{\mathrm{Ag}} - \varepsilon_{\mathrm{air}}}{\varepsilon_{\mathrm{air}} + L_k(\varepsilon_{\mathrm{Ag}} - \varepsilon_{\mathrm{air}})}\right) \quad \text{for } k=1,2 \tag{4.4}$$

where k =1 corresponds to the primary extraordinary case (to be discussed in section 4.6.2) and k = 2 corresponds to the ordinary case. L_k is the depolarization factor which depends on the shape and geometry of the nanorods. Here the nanorods are assumed to have a prolate spheroid shape, and hence L_k is given by

$$L_1 = \frac{1-e^2}{e^2}\left[\frac{1}{2e}\ln\left(\frac{1+e}{1-e}\right)-1\right] \quad , e = \sqrt{1-(d/l)^2} \tag{4.5}$$

$$L_2 = \frac{(1-L_1)}{2} \tag{4.6}$$

Here *d* and *l* are the average diameter and length of the AgNRs, respectively. Based on these calculations, we obtained n_{E} =0.203+2.92i and n_{O} =1.62+0.0106i for the values of refractive indices for primary extraordinary and ordinary waves, respectively. Here $i = \sqrt{-1}$, denoting the unity imaginary complex number.

4.6.2 Anisotropic behavior of AgNRs

AgNR arrays, due to their high-aspect ratio geometry, belong to a class of anisotropic materials called uniaxial materials [80], which have a single axis of anisotropy as compared to biaxial materials with more than 1 axis of anisotropy. For uniaxial materials, light with linear polarizations parallel or perpendicular to the optical axis has unequal dielectric functions and hence different refractive indices. Incident waves with $\mathbf{H}$ perpendicular to $\hat{\mathbf{c}}$ are called extraordinary waves while waves with $\mathbf{E}$ perpendicular to $\hat{\mathbf{c}}$ are classified as ordinary waves. However, there exists a special case when both $\mathbf{H}$ is perpendicular to $\hat{\mathbf{c}}$ and $\mathbf{E}$ is parallel to $\hat{\mathbf{c}}$, which is called the primary

extraordinary wave. Extraordinary waves provide a metallic like effect whereas ordinary waves provide a dielectric like effect. Schematic of a single AgNR is shown in fig. 4.4.

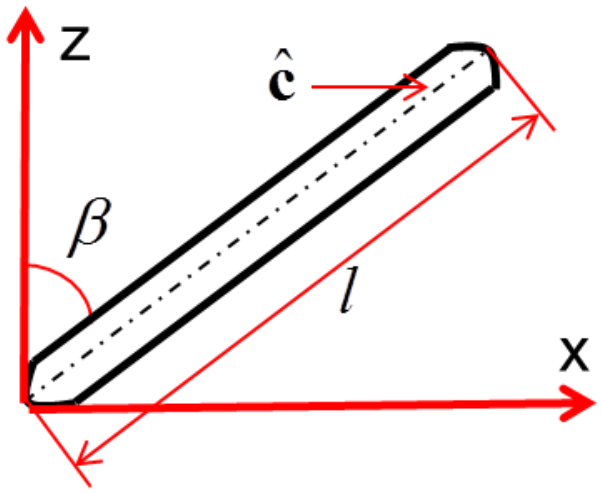

Figure 4.4 Schematic of single Silver Nanorod (AgNR) depicting its optical axis $(\hat{\mathbf{c}})$, length (l) and inclination angle (β) with respect to Z axis.

In general, at anisotropic interfaces, pure TE and TM waves do not exist. This is due to coupling between the ordinary and extraordinary waves which occurs at these interfaces [81]. Polarization decoupling occurs when one of the principal axes of the permittivity tensor of both regions is normal to the plane of incidence. In other words, polarization decoupling occurs when the optical axis either lies in the plane of incidence or is perpendicular to it. Therefore, if the optical axis lies in the plane of incidence, the ordinary and extraordinary waves correspond to TE and TM polarizations, respectively. On the other hand, when the optical axis is perpendicular to the plane of incidence, ordinary and extraordinary waves correspond to TM and TE polarizations, respectively.

For sample 1, when AgNR projections are perpendicular to CD grooves, optical axis lies in the plane of incidence, and hence coupling is not a problem. For TE polarization, **E** is perpendicular to $\hat{\mathbf{c}}$ for both reflected and refracted waves. Hence TE polarization corresponds to ordinary waves. However, for TM polarization (**H** perpendicular to $\hat{\mathbf{c}}$), at normal incidence, **E** is parallel to $\hat{\mathbf{c}}$ only if $\beta = 90$ degrees. Also, the parallel condition holds only for specular reflection or 0^{th} order diffraction only. For other orders **E** and $\hat{\mathbf{c}}$ are not truly parallel. Hence TM waves behave as *general* extraordinary waves. For RCWA calculation, the use of optical constants for primary extraordinary waves for this case will result in some deviation from measured experimental values.

For sample 2, when AgNR projections are parallel to CD grooves, optical axis lies neither in the plane of incidence nor in the plane perpendicular to it. Hence, extraordinary and ordinary waves are coupled to each other and pure TE and TM polarizations do not exist for this case. However, if we tilt the rods such that $\beta = 90$ degrees, then the optical axis becomes perpendicular to the plane of incidence, thus uncoupling the polarizations. For TE polarization both **H** and **E** becomes perpendicular and parallel to $\hat{\mathbf{c}}$, respectively and hence results in a primary extraordinary wave. For TM polarization, **E** is perpendicular to $\hat{\mathbf{c}}$ and hence results in an ordinary wave.

To include the effect of coupling in our calculations, we add a small portion (2 percent) of ordinary wave property to the extraordinary wave property for TE polarization of sample 2 as well as add 2 percent of extraordinary wave property to the ordinary wave property for the TM polarization of the same sample. This approach does not produce any appreciable change in the optical constants used for TE polarization;

however by doing so, the extinction coefficient for TM waves increases to 0.3. Table 4.2 below summarizes the final refractive indices used in the coupled-wave analysis.

Table 4.2 Refractive indices for each sample and polarization

Sample 1		**Sample 2**	
TE	TM ($\beta = 90^o$)	TE ($\beta = 90^o$ degrees)	TM ($\beta = 90^o$ degrees)
$1.62+0.0106\,i$	$0.203+2.92\,i$	$0.203+2.92\,i$	$1.62+0.03\,i$

To conclude this section, besides the parameters discussed above which affect the optical constants and radiative properties of AgNRs, some other parameters such as surface roughness, non-uniform deposition, nanorod shapes etc., which play a major role to the diffraction behavior of these samples, are very challenging to be quantified by pure numerical analysis.

4.7 RCWA Calculation

For RCWA calculation, the approach suggested by Moharam et al [49, 50] is followed. The method of calculation has already been outlined in section 4.2. For reference please see Fig. 2.1. A 635-nm beam of linearly polarized light falls on the sample (medium 2) from air (medium 1), at near normal incidence. Medium 3 is the semi-infinite CD substrate (made of polycarbonate) with a frequency independent refractive index of n_{CD}=1.6. The optical constants of gold layer on CD are obtained from tabulated data [69]. Medium 2 is a grating layer which is periodic and heterogeneous in nature. The gratings consist of AgNRs while space between 2 successive AgNRs is filled

with air. The optical constants of AgNR-air layer are modeled by EMT as shown in previous sections. For the purposes of RCWA analysis, it is assumed that the AgNR layer behaves like an isotropic medium. This approximation causes the calculated values to deviate from the measured values, but within the limits of reasonableness. Sample 1 is modeled by using a combination of rectangle and triangle shaped profiles, while sample 2 is modeled by a rectangular profile throughout, as shown in the fig. 4.5.

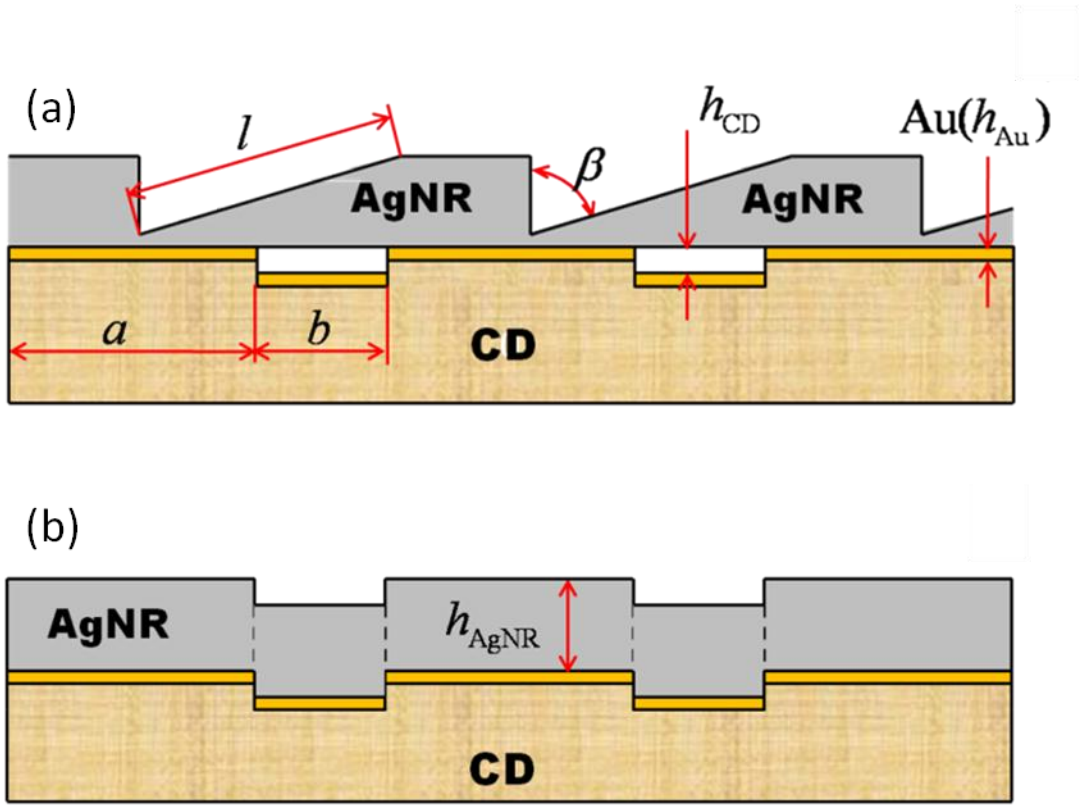

Fig 4.5(a) Sample 1 geometry: l =1.2 um, h_{CD} = 0.1 um, h_{Au} = 0.05 um, a = 0.9 um, b = 0.6 um, β =70 degrees (b) Sample 2 geometry: $h_{AgNR} = l\cos(\beta)$

The triangular profile is approximated as the superposition of 100 rectangular slices with equal height but varying widths, as illustrated in section 4.2. The widths are

non-dimensionalized with respect to grating period and converted to filling fractions (f) for each layer, which forms a vital input to the RCWA code. RCWA analysis for rectangular slices by RCWA follows the usual approach. For both samples, 161 Fourier diffraction orders are used. The following paragraphs outline the detailed geometries and computational parameters for each sample.

Sample 1:

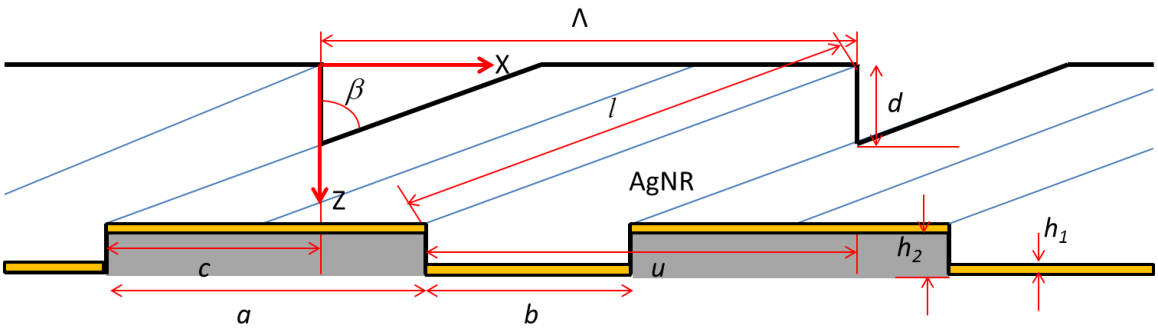

Figure 4.6 Detailed geometry of sample 1. The actual nanorods are shown as blue colored lines, while the AgNR grating profile is drawn with a solid black line. The gold coating is shown in yellow color.

Calculation of Parameters: From fig. 4.6,

$$u = l\cos(90-\beta) \tag{4.7}$$

$$c = u - b \tag{4.8}$$

$$d = l\sin(90-\beta) - c\tan(90-\beta) \tag{4.9}$$

In the region 0<Z<d: The AgNR profile is divided into *M* layers of equal thickness, such that the vertical edge of each layer bisects the original profile. This is shown in fig. 4.7.

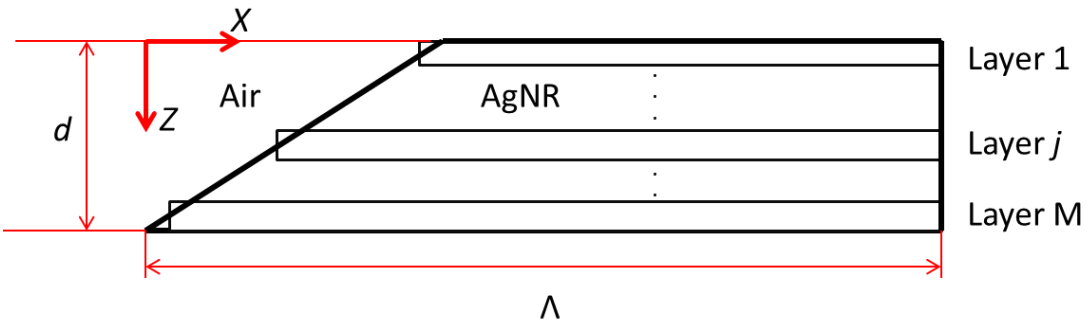

Figure 4.7 Approximation of triangular profile with multiple rectangular slices

For layer j, let its height be denoted by h_j and distance of its left edge from the origin denoted by x_j. From Eq. (2.22), $h_j = \frac{d}{M}$ since all layers have the same thickness. The left abscissa for the j th layer is given by

$$x_j = \left((M-j)h_j + \frac{h_j}{2}\right)\tan(\beta) = \left(2(M-j)+1\right)\frac{d\tan(\beta)}{2M} \tag{4.10}$$

Thus, non-dimensional filling fraction for the left edge of j th layer of AgNR $\left(f_{1,j}\right) = \frac{x_j}{\Lambda}$ and that for the right edge of j th layer of AgNR $\left(f_{2,j}\right) = 1$. Similarly, filling fractions for the other layers are calculated and listed in Table 4.3. Note that $f1$ corresponds to the normalized position of left edge of a material in a particular layer and $f2$ corresponds to the normalized position of right edge of the same material in that layer.

Table 4.3 Filling fractions for each layer for sample 1. The quantity in the brackets in each cell denotes the material that the filling fraction is applicable for. For a binary grating, filling fraction of the second material in the each layer can be calculated by subtracting the cell value of that layer from the grating period Λ

Filling Fraction	**Z limits of layers**			
	$0 < Z < d$	$d < Z < l\sin(90-\beta)$	$l\sin(90-\beta) < Z < l\sin(90-\beta)+h_2$	$l\sin(90-\beta)+h_2 < Z < l\sin(90-\beta)+h_1+h_2$
$f1$ (left abscissa)	$\frac{x_j}{\Lambda}$ (AgNR)	1 (AgNR)	$\frac{(a-c)}{\Lambda}$ (Air)	$\frac{(a-c)}{\Lambda}$ (Au)
$f2$ (right abscissa)	1 (AgNR)	1 (AgNR)	$\frac{(\Lambda-c)}{\Lambda}$ (Air)	$\frac{(\Lambda-c)}{\Lambda}$ (Au)

These values of $f1$, $f2$ along with relevant optical constants of each layer are input into the RCWA code.

Sample 2

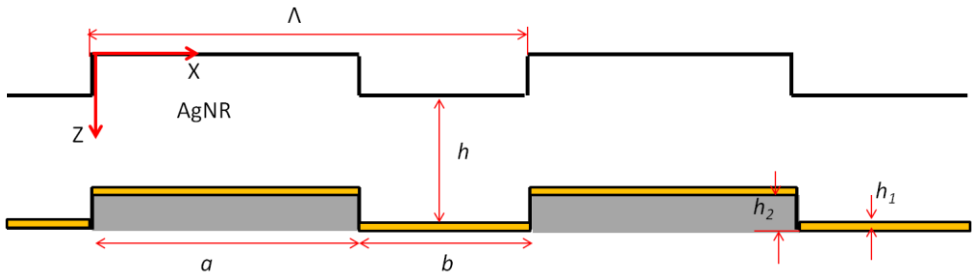

Figure 4.8 Detailed geometry of sample 2. The AgNR profile is outlined in solid black lines. The gold coating is shown in yellow color.

From fig. 4.8,

$$h = l\sin(90-\beta) \tag{1.11}$$

Similar to sample 1, the filling fractions of each layer is calculated as a function of its Z coordinate and listed in Table 4.4. $f1$ corresponds to the filling fraction for the left edge of a material in a particular layer and $f2$ corresponds to the filling fraction for the right edge of the same material in the same layer.

Table 4.4 Filling fractions for each layer for sample 2. The quantity in the brackets in each cell denotes the material that the filling fraction is applicable for. For a binary grating, filling fraction of the second material in the each layer can be calculated by subtracting the cell value of that layer from the grating period Λ.

Filling Fraction	**Z limits of layers**				
	$0 < Z < h_2$	$h_2 < Z < h$	$h < Z < h + h_1$	$h + h_1 < Z < h + h_2$	$h + h_2 < Z < h + h_1 + h_2$
$f1$ (left abscissa)	0 (AgNR)	0 (AgNR)	0 (Au)	0 (CD)	$\frac{a}{\Lambda}$ (Au)
$f2$ (right abscissa)	$\frac{a}{\Lambda}$ (AgNR)	1 (AgNR)	$\frac{a}{\Lambda}$ (Au)	$\frac{a}{\Lambda}$ (CD)	1 (Au)

4.8 Results and Analysis

RCWA predicted values of reflectance are plotted together with the measured values (Meas) for both samples in Fig. 4.9, for trend analysis of diffraction energy of different orders, denoted by R_{peak}. Based on the grating eq. (2.4), it is found that diffraction by the AgNR samples results in 5 diffraction orders ($m = \pm 2, \pm 1$ and 0). Reflectance for all 5 diffraction orders are calculated and plotted in form of bar-graphs with corresponding measurement values for comparison.

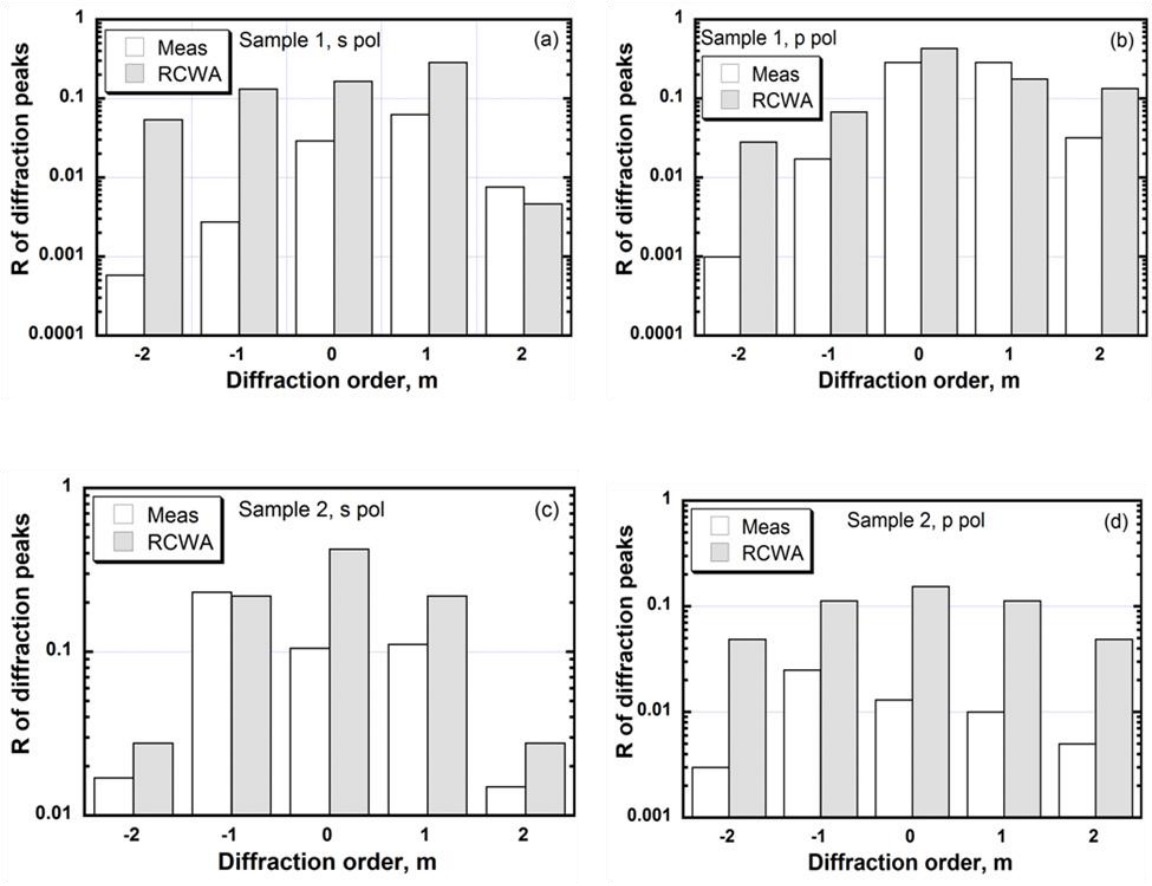

Figure 4.9 Plots (on log scale) comparing the RCWA calculated values (RCWA) with Measurements (Meas) for (a) Sample 1, TE pol. (b) Sample 1, TM pol. (c) Sample 2, TE pol. (d) Sample 2, TM pol.

For sample 1, for which the relevant figures are 4.9 (a) and 4.9(b), there is good agreement between theory and experiment for TE polarization while a reasonably good agreement is evident for TM polarization.For both measurements and RCWA calculation, positive diffraction orders have higher energy than negative diffraction orders due the geometry of the grating. The higher predicted value of R_{peak} for zeroth order TM polarized wave could be due to anisotropic properties of the AgNR layer which is difficult to incorporate into the RCWA model. For Sample 2, the rectangular profile results in a symmetric power distribution of diffraction peaks with respect to *m*=0, which agrees with the measurement trend by neglecting the experiment uncertainties and sample non-uniformity. A comparison is made between the DHR measurements performed by IS and R_{total} computation carried out by RCWA, and is presented in table 4.5. Here R_{total} is the sum of R_{peak}'s from all five diffraction orders as computed by RCWA.

Table 4.5 Comparison of total reflection between IS measurements (DHR) and RCWA calculations (R_{total})

Total Reflectance	**Sample 1**		**Sample 2**	
	TE	TM	TE	TM
RCWA(R_{total} **)**	0.643	0.835	0.917	0.476
IS (DHR)	0.577	0.876	0.870	0.463

From Table 4.5, the predicted R_{total} agree well with corresponding DHR measurements from IS with the largest absolute difference being less than 0.07. The

differences are caused by the uncertainties from modeling such as the unaccounted effects of geometry, anisotropy, and coupling, as well as the uncertainty from IS measurements. In general, R_{total} values are higher, which might be due to the signal loss from the entrance and back ports of the IS. However, for the exceptional case of sample 1 with TM polarization R_{total} is lower than DHR, which may be due to the fact that the RCWA calculation does not consider the sample anisotropy as discussed earlier.

It should be noted that RCWA analysis is valid for smooth surfaces only, and does not take the sample nonuniformity into account. Because of this, scattering or diffuse energy components cannot be calculated via this analysis. To implicitly include the effect of scattering caused by AgNR arrays, the scattering rate of bulk silver has been modified to 10 times of its original value as used by Modest. Based on this modification, one can calculate the optical properties of AgNR-air effective layer and then use them to calculate their radiative properties. The total reflectance values calculated by RCWA are then compared with the experimental results and good agreement was observed. The factor of 10 was so chosen that one is able to obtain good agreements for both reflectance trends and overall reflectance values. In this manner, the effect of scattering is included in RCWA calculations in an implicit manner.

CHAPTER 5

CONCLUSION

Micro/nanostructures, through control of their thermal radiative properties, can be very useful in energy, biochemistry and optics related fields. They can act as diffraction gratings in monochromators and spectrophotometers, act as sensors in identification of biological virus strains and act as resonators and filters to trap or transmit light energy, respectively. Rigorous coupled-wave analysis is used to perform a numerical investigation of the radiative responses of these structures.

Inclined parallel plate grating arrays were used to demonstrate the resonator characteristics of micro/nanostructures. These structures captured incident light at certain wavelengths, corresponding to resonance wavelengths of magnetic polaritons and surface plasmon polaritons. Electromagnetic field distribution and spectral-directional contour plots computed by RCWA confirmed the presence of these mechanisms. Analytical confirmation was provided by LC circuit model. Effects of variation of different geometrical parameters on the resonator behavior were studied through both RCWA and LC circuit models.

Obliquely aligned silver nanorod arrays were used to demonstrate unique optical properties of nanostructures that exhibit remarkably distinct responses to different light polarizations and different nanorod orientations. These arrays, grown on compact disc gratings, consist of high-aspect ratio nanorods which endow them with the property of birefringency, leading to two types of behavior to incident light: dielectric and metallic corresponding to ordinary and extraordinary waves, respectively. RCWA studies were

performed on nanorods-on-gratings structure to determine the peak diffraction efficiencies for individual orders. Trends of these values were compared against the measurements. Also peak total reflection values from RCWA was compared against the DHR measurements taken by IS. Both comparisons resulted in good agreements.

This thesis demonstrated that structural geometries of microstructures can have significant effects on their radiative properties. On the basis of present work, a more detailed study can be considered in the future whereby additional geometries and a wider wavelength spectrum can be included to predict their effects on the radiative properties. The study can also be used to investigate the directional and spectral dependence of their optical responses, which in turn can be used to fine-tune the design of relevant applications. These micro/nanostructures promise to deliver better solutions in the design of energy efficient applications in the future.

REFERENCES

[1] Wang, W. S., Zhen, L., Xu, C. Y., and Shao, W. Z., 2008, "Hollow inorganic micro/nanostructures synthesized by solution-phase method," Polymer Chemistry Papers, 20(5), pp. 679-689.

[2] Basu, S., Chen, Y. B., and Zhang, Z. M., 2007, "Microscale radiation in thermophotovoltaic devices—A review," International Journal of Energy Research, 31(6-7), pp. 689-716.

[3] Zhang, Z. M., 2007, Nano/microscale heat transfer, McGraw-Hill, New York.

[4] Driskell, J. D., et al., 2008, "The use of aligned silver nanorod arrays prepared by oblique angle deposition as surface enhanced Raman scattering substrates," The Journal of Physical Chemistry C, 112(4), pp. 895-901.

[5] Fu, J., Park, B., and Zhao, Y., 2009, "Nanorod-mediated surface plasmon resonance sensor based on effective medium theory," Applied Optics, 48(23), pp. 4637-4649.

[6] Xu, F., et al., 2011, "Silver nanoparticles coated zinc oxide nanorods array as superhydrophobic substrate for the amplified SERS effect," The Journal of Physical Chemistry C, 115(20), pp. 9977-9983.

[7] Gaylord, T. K., and Moharam, M., 1985, "Analysis and applications of optical diffraction by gratings," Proceedings of the IEEE, 73(5), pp. 894-937.

[8] Kneubühl, F., 1969, "Diffraction grating spectroscopy," Applied Optics, 8(3), pp. 505-519.

[9] Jones, M. L., Kenan, R. P., and Verber, C. M., 1995, "Rectangular characteristic gratings for waveguide input and output coupling," Applied Optics, 34(20), pp. 4149-4158.

[10] Takahashi, H., Hibino, Y., and Nishi, I., 1992, "Polarization-insensitive arrayed-waveguide grating wavelength multiplexer on silicon," Optics Letters, 17(7), pp. 499-501.

[11] Treacy, E., 1969, "Optical pulse compression with diffraction gratings," Quantum Electronics, IEEE Journal of, 5(9), pp. 454-458.

[12] Boyd, R., et al., 1995, "High-efficiency metallic diffraction gratings for laser applications," Applied Optics, 34(10), pp. 1697-1706.

[13] Nevière, M., 2000, Electromagnetic resonances in nonlinear optics, CRC.

[14] Reinisch, R., and Nevière, M., 1983, "Electromagnetic theory of diffraction in nonlinear optics and surface-enhanced nonlinear optical effects," Physical Review B, 28(4), pp. 1870-1885.

[15] Yablonovitch, E., 1987, "Inhibited spontaneous emission in solid-state physics and electronics," Physical Review Letters, 58(20), pp. 2059-2062.

[16] Sheng, P., Bloch, A., and Stepleman, R., 1983, "Wavelength selective absorption enhancement in thin film solar cells," Applied Physics Letters, 43(6), pp. 579-581.

[17] Cadilhac, M., and Neviere, M., 1971, "Diffraction of a plane electromagnetic wave by an infinitely conductive grating, when the incident wave vector is not orthogonal relative to the grooves(Plane electromagnetic wave diffraction by infinitely conductive grating at nonorthogonal incidence angles, using conformal mapping technique)," Optics Communications, 4, pp. 13-18.

[18] Neviere, M., Petit, R., and Cadilhac, M., 1973, "About the theory of optical grating coupler-waveguide systems," Optics Communications, 8(2), pp. 113-117.

[19] Nevière, M., Vincent, P., and Petit, R., 1974, "Theory of conducting gratings and their applications to optics," Nouvelle Revue d'Optique, 5(2), pp. 65-77.

[20] Maystre, D., and Petit, R., 1972, "Diffraction par un reseau lamellaire infiniment conducteur," Optics Communications, 5(2), pp. 90-93.

[21] Petersen, H., 1982, "The plane grating and elliptical mirror: a new optical configuration for monochromators," Optics Communications, 40(6), pp. 402-406.

[22] Loewen, E., Neviere, M., and Maystre, D., 1977, "Grating efficiency theory as it applies to blazed and holographic gratings," Applied Optics, 16(10), pp. 2711-2721.

[23] Mashev, L., and Popov, E., 1984, "Diffraction efficiency anomalies of multicoated dielectric gratings," Optics Communications, 51(3), pp. 131-136.

[24] Sauer, F., 1989, "Fabrication of diffractive—reflective optical interconnects for infrared operation based on total internal reflection," Applied Optics, 28(2), pp. 386-388.

[25] Martin-Moreno, L., et al., 2001, "Theory of extraordinary optical transmission through subwavelength hole arrays," Physical Review Letters, 86(6), pp. 1114-1117.

[26] Porto, J., Garcia-Vidal, F., and Pendry, J., 1999, "Transmission resonances on metallic gratings with very narrow slits," Physical Review Letters, 83(14), pp. 2845-2848.

[27] Pertsch, T., et al., 2004, "Discrete diffraction in two-dimensional arrays of coupled waveguides in silica," Optics Letters, 29(5), pp. 468-470.

[28] Baida, F., and Van Labeke, D., 2002, "Light transmission by subwavelength annular aperture arrays in metallic films," Optics Communications, 209(1-3), pp. 17-22.

[29] Li, T., et al., 2007, "Exploring magnetic plasmon polaritons in optical transmission through hole arrays perforated in trilayer structures," Applied Physics Letters, 90(25), pp. 251112-251114.

[30] Li, T., et al., 2008, "Dispersion of magnetic plasmon polaritons in perforated trilayer metamaterials," Journal of Applied Physics, 103(2), pp. 023104-0123107.

[31] Wang, L., and Zhang, Z. M., 2010, "Effect of magnetic polaritons on the radiative properties of double-layer nanoslit arrays," Journal of Optical Society of America B, 27(12), pp. 2595-2604.

[32] Lee, B., Chen, Y. B., and Zhang, Z., 2008, "Confinement of infrared radiation to nanometer scales through metallic slit arrays," Journal of Quantitative Spectroscopy and Radiative Transfer, 109(4), pp. 608-619.

[33] Lee, B., Chen, Y., and Zhang, Z., 2008, "Transmission enhancement through nanoscale metallic slit arrays from the visible to mid-infrared," Journal of Computational and Theoretical Nanoscience, 5(2), pp. 201-213.

[34] Robbie, K., and Brett, M., 1997, "Sculptured thin films and glancing angle deposition: Growth mechanics and applications," Journal of Vacuum Science & Technology A: Vacuum, Surfaces, and Films, 15(3), pp. 1460-1465.

[35] Zhang, H., Chung, S. W., and Mirkin, C. A., 2003, "Fabrication of sub-50-nm solid-state nanostructures on the basis of dip-pen nanolithography," Nano Letters, 3(1), pp. 43-45.

[36] Zhao, X. M., Xia, Y., and Whitesides, G. M., 1997, "Soft lithographic methods for nano-fabrication," Journal of Materials Chemistry, 7(7), pp. 1069-1074.

[37] Li, Y., Cai, W., and Duan, G., 2007, "Ordered Micro/Nanostructured Arrays Based on the Monolayer Colloidal Crystals†," Chemistry of Materials, 20(3), pp. 615-624.

[38] Meecham, W. C., 1956, "Variational Method for the Calculation of the Distribution of Energy Reflected from a Periodic Surface. I," Journal of Applied Physics, 27(4), pp. 361-367.

[39] Harrison, G. R., and Stroke, G. W., 1960, "Attainment of high resolution with diffraction gratings and echelles," Journal of Optical Society of America, 50(12), pp. 1153-1157.

[40] Moharam, M., and Gaylord, T., 1981, "Rigorous coupled-wave analysis of planar-grating diffraction," Journal of Optical Society of America, 71(7), pp. 811-818.

[41] Moharam, M., and Gaylord, T., 1986, "Rigorous coupled-wave analysis of metallic surface-relief gratings," Journal of Optical Society of America A, 3(11), pp. 1780-1787.

[42] Moharam, M., and Gaylord, T., 1983, "Three-dimensional vector coupled-wave analysis of planar-grating diffraction," Journal of Optical Society of America, 73(9), pp. 1105-1112.

[43] Moharam, M., and Gaylord, T., 1982, "Diffraction analysis of dielectric surface-relief gratings," Journal of Optical Society of America, 72(10), pp. 1385-1392.

[44] Petit, R., and Tayeb, G., 1990, "Theoretical and numerical study of gratings consisting of periodic arrays of thin and lossy strips," Optics Communications, 7(9), pp. 1686-1692.

[45] Li, L., 1996, "Formulation and comparison of two recursive matrix algorithms for modeling layered diffraction gratings," Journal of Optical Society of America A, 13(5), pp. 1024-1035.

[46] Lalanne, P., and Morris, G. M., 1996, "Highly improved convergence of the coupled-wave method for TM polarization," Journal of the Optical Society of America A, 13(4), pp. 779-784.

[47] Li, L., 1996, "Use of Fourier series in the analysis of discontinuous periodic structures," Journal of Optical Society of America A, 13(9), pp. 1870-1876.

[48] Li, L., 1993, "Multilayer modal method for diffraction gratings of arbitrary profile, depth, and permittivity," Journal of Optical Society of America A, 10(12), pp. 2581-2591.

[49] Moharam, M., Grann, E. B., Pommet, D. A., and Gaylord, T., 1995, "Formulation for stable and efficient implementation of the rigorous coupled-wave analysis of binary gratings," Journal of Optical Society of America A, 12(5), pp. 1068-1076.

[50] Moharam, M., Pommet, D. A., Grann, E. B., and Gaylord, T., 1995, "Stable implementation of the rigorous coupled-wave analysis for surface-relief gratings: enhanced transmittance matrix approach," Journal of Optical Society of America A, 12(5), pp. 1077-1086.

[51] Hava, S., and Auslender, M., 2000, "Design and analysis of low-reflection grating microstructures for a solar energy absorber," Solar Energy Materials and Solar Cells, 61(2), pp. 143-151.

[52] Estrada-Gasca, C., Alvarez-Garcia, G., and Nair, P., 1993, "Theoretical analysis of the thermal performance of chemically deposited solar control coatings," Journal of Physics D: Applied Physics, 26(8), pp. 1304-1309.

[53] Tonon, C., Duvignacq, C., Teyssedre, G., and Dinguirard, M., 2001, "Degradation of the optical properties of ZnO-based thermal control coatings in simulated space environment," Journal of Physics D: Applied Physics, 34(1), pp. 124-130.

[54] Sai, H., Yugami, H., Akiyama, Y., Kanamori, Y., and Hane, K., 2001, "Spectral control of thermal emission by periodic microstructured surfaces in the near-infrared region," Journal of Optical Society of America A, 18(7), pp. 1471-1476.

[55] Hesketh, P. J., Zemel, J. N., and Gebhart, B., 1988, "Polarized spectral emittance from periodic micromachined surfaces. I. Doped silicon: the normal direction," Physical Review B, 37(18), pp. 10795-10802.

[56] Hesketh, P. J., Zemel, J. N., and Gebhart, B., 1988, "Polarized spectral emittance from periodic micromachined surfaces. II. Doped silicon: angular variation," Physical Review B, 37(18), pp. 10803-10813.

[57] Wang, T., and Zemel, J. N., 1991, "Polarized spectral emittance from periodic micromachined surfaces--III. Undoped silicon: The normal direction in shallow lamellar gratings," Infrared Physics, 32, pp. 477-488.

[58] Wang, T., and Zemel, J. N., 1992, "Polarized spectral emittance from periodic micromachined surfaces: IV. Undoped silicon: Normal direction in deep lamellar gratings," Applied Optics, 31(6), pp. 732-736.

[59] Buckius, K. T. R. O., 1998, "Bi-directional reflection measurements from two-dimensional microcontoured metallic surfaces," Nanoscale and Microscale Thermophysical Engineering, 2(4), pp. 245-260.

[60] Heinzel, A., Boerner, V., Gombert, A., Wittwer, V., and Luther, J., 1999, "Microstructured tungsten surfaces as selective emitters," AIP Conf. Proc., 460(1), pp. 191-196.

[61] Zayats, A. V., Smolyaninov, I. I., and Maradudin, A. A., 2005, "Nano-optics of surface plasmon polaritons," Physics Reports, 408(3-4), pp. 131-314.

[62] Byun, K. M., Shuler, M. L., Kim, S. J., Yoon, S. J., and Kim, D., 2008, "Sensitivity enhancement of surface plasmon resonance imaging using periodic metallic nanowires," Journal of Lightwave Technology, 26(11), pp. 1472-1478.

[63] Hearty, S., Leonard, P., Quinn, J., and O'Kennedy, R., 2006, "Production, characterisation and potential application of a novel monoclonal antibody for rapid

identification of virulent Listeria monocytogenes," Journal of Microbiological Methods, 66(2), pp. 294-312.

[64] Hessel, A., and Oliner, A., 1965, "A new theory of Wood's anomalies on optical gratings," Applied Optics, 4(10), pp. 1275-1297.

[65] Cornet, P., Chandezon, J., and Faure, C., 1997, "Conical diffraction of a plane wave by an inclined parallel-plate grating," Journal of Optical Society of America A, 14(2), pp. 437-449.

[66] Kobayashi, K., and Inoue, T., 1988, "Diffraction of a plane wave by an inclined parallel plate grating," Antennas and Propagation, IEEE Transactions on, 36(10), pp. 1424-1434.

[67] Kobayashi, K., and Sawai, A., 1992, "Plane wave diffraction by an open-ended parallel plate waveguide cavity," Journal of Electromagnetic Waves and Applications, 6, 1(6), pp. 475-512.

[68] Modest, M. F., 2003, Radiative heat transfer, Academic Press, USA.

[69] Palik, E. D., and Ghosh, G., 1998, Handbook of optical constants of solids, Academic Press, USA.

[70] Wang, L., and Zhang, Z., 2011, "Phonon-mediated magnetic polaritons in the infrared region," Optics Express, 19(102), pp. A126-A135.

[71] Laroche, T., and Girard, C., 2006, "Near-field optical properties of single plasmonic nanowires," Applied Physics Letters, 89(23), p. 233119-233121.

[72] Silveirinha, M. G., Belov, P. A., and Simovski, C. R., 2007, "Subwavelength imaging at infrared frequencies using an array of metallic nanorods," Physical Review B, 75(3), pp. 035108-035119.

[73] Zhao, Y., et al., 1997, "Silver nanorod arrays can distinguish virus strains," Physics Review Letters, 78, pp. 1667-1670.

[74] Shen, Y., Zhu, Q., and Zhang, Z., 2003, "A scatterometer for measuring the bidirectional reflectance and transmittance of semiconductor wafers with rough surfaces," Review of Scientific Instruments, 74(11), pp. 4885-4892.

[75] Zhou, Y., Shen, Y., Zhang, Z., Tsai, B., and DeWitt, D., 2002, "A Monte Carlo model for predicting the effective emissivity of the silicon wafer in rapid thermal processing furnaces," International Journal of Heat and Mass Transfer, 45(9), pp. 1945-1949.

[76] Zhou, Y., and Zhang, Z., 2003, "Radiative properties of semitransparent silicon wafers with rough surfaces," Journal of Heat Transfer, 125(3), pp. 462-470.

[77] Zhou, Y., Zhang, Z., DeWitt, D., and Tsai, B., 2001, "Effects of radiative properties of surfaces on radiometric temperature measurement," Advanced Thermal Processing of Semiconductors 9th International Conference on RTP, IEEE, pp. 179-188.

[78] Li, Q., Lee, B. J., Zhang, Z. M., and Allen, D. W., 2008, "Light scattering of semitransparent sintered polytetrafluoroethylene films," Journal of Biomedical Optics, 13(5), pp. 054064(1-12).

[79] Choy, T. C., 1999, Effective medium theory: principles and applications, Oxford University Press, USA.

[80] Azzam, R., and Bashara, N., 1972, "Simplified approach to the propagation of polarized light in anisotropic media—application to liquid crystals," Journal of Optical Society of America, 62(11), pp. 1252-1257.

[81] Knoesen, A., Moharam, M., and Gaylord, T., 1985, "Electromagnetic propagation at interfaces and in waveguides in uniaxial crystals," Applied Physics B: Lasers and Optics, 38(3), pp. 171-178.